TU Delft

Delft University of Technology

Document Version
Final published version

Licence
CC BY-NC

Citation (APA)
Yang, Y., Sigmundsson, F., Geirsson, H., Biggs, J., Drouin, V., Sepúlveda-Araya, J., Hreinsdóttir, S., Lanzi, C., Gottsmann, J., Broerse, T., & Verhagen, S. (2026). Plate Divergence at the Krafla Volcanic System, Iceland: Insight From GNSS Geodesy and Sentinel-1 Satellite Radar Interferometry in 2002–2024. *Journal of Geophysical Research: Solid Earth*, *131*(8), Article e2026JB034040. https://doi.org/10.1029/2026JB034040

Important note
To cite this publication, please use the final published version (if applicable).
Please check the document version above.

Copyright
In case the licence states “Dutch Copyright Act (Article 25fa)”, this publication was made available Green Open Access via the TU Delft Institutional Repository pursuant to Dutch Copyright Act (Article 25fa, the Taverne amendment). This provision does not affect copyright ownership.
Unless copyright is transferred by contract or statute, it remains with the copyright holder.

Sharing and reuse
Other than for strictly personal use, it is not permitted to download, forward or distribute the text or part of it, without the consent of the author(s) and/or copyright holder(s), unless the work is under an open content license such as Creative Commons.

Takedown policy
Please contact us and provide details if you believe this document breaches copyrights.
We will remove access to the work immediately and investigate your claim.

This work is downloaded from Delft University of Technology.

Check for updates

JGR Solid Earth

RESEARCH ARTICLE
10.1029/2026JB034040

Plate Divergence at the Krafla Volcanic System, Iceland: Insight From GNSS Geodesy and Sentinel-1 Satellite Radar Interferometry in 2002–2024

Yilin Yang[1,2], Freysteinn Sigmundsson[1], Halldór Geirsson[1], Juliet Biggs[3], Vincent Drouin[4], Josefa Sepúlveda-Araya[5], Sigrún Hreinsdóttir[6], Chiara Lanzi[4], Joachim Gottsmann[7], Taco Broerse[8], and Sandra Verhagen[8]

[1]Nordic Volcanological Center, Institute and Faculty of Earth Sciences, University of Iceland, Reykjavík, Iceland, [2]Now at: Earthquake Research Institute, The University of Tokyo, Tokyo, Japan, [3]COMET, School of Earth Sciences, University of Bristol, Bristol, UK, [4]Icelandic Meteorological Office, Reykjavík, Iceland, [5]COMET, School of Earth and Environment, University of Leeds, Leeds, UK, [6]GNS Science, Lower Hutt, New Zealand, [7]Department of Earth and Environmental Sciences, Ludwig-Maximilians-Universität München, Munich, Germany, [8]Faculty of Civil Engineering and Geosciences, Delft University of Technology, Delft, The Netherlands

Abstract The Krafla volcanic system in Iceland, a subaerial segment of the divergent boundary between the North American and Eurasian plates, offers a unique opportunity to investigate volcano-tectonic processes. We present a six-segment kinematic back slip plate boundary model constrained jointly by long-term deformation velocity fields from Global Navigation Satellite System (2002–2024) and Sentinel-1 SAR interferograms (2015–2023). The inferred plate boundary axis passes through the middle of the Krafla caldera and follows recent eruptive fissures. Its orientation varies between N1.2°–N10.8°E within and south of the central volcano but rotates to NNW-SSE north of it. For this preferred axis geometry, the inferred spreading rate is $19.2^{+0.2}_{-0.2}$ mm/yr in an azimuth of $283.5^{+0.2}_{-0.2}$° (formal uncertainties corresponding to 95% confidence interval of the Bayesian inversion results). Locking depth varies significantly along the plate boundary axis: it is shallowest within and just north of the Krafla caldera ($2.71^{+0.16}_{-0.16}$ km) and deepens to $4.86^{+0.20}_{-0.10}$ and $6.79^{+0.27}_{-0.26}$ km to the north and south, respectively. This variation is consistent with the depth distribution of seismicity and reflects an up-doming brittle-ductile transition along the fissure swarm. These first-order features remain robust, although uncertainties increase when the axis location is allowed to vary. After correcting vertical velocities for glacial isostatic adjustment and regional subsidence caused by extensional rheological anomalies, residual velocities reveal three areas of local deflation: two related to the Krafla and Bjarnarflag geothermal fields and one at the northernmost part of the 1975–1984 Krafla lava field. Therefore, detailed plate boundary models can provide insights into crustal rheology, volcano-tectonic interactions and local processes.

Plain Language Summary At tectonic plate boundaries, shallow crust can be locked, allowing strain to accumulate before being released in earthquakes or affecting volcanic activity. The Krafla volcanic system in northeast Iceland lies along the extensional boundary between the North American and Eurasian plates, making it an ideal setting to study interactions between plate spreading and volcanism. We analyze more than two decades of Global Positioning System measurements (2002–2024) together with Sentinel-1 radar images (2015–2023) to quantify long-term ground motion at Krafla. Using elastic modeling of the surface velocity field, we resolve the geometry of the plate boundary axis and estimate the locking depth of the crust. The locking depth is shallowest beneath the Krafla caldera and just north of it, indicating more localized deformation in this area. This suggests that volcanic and geothermal activity may weaken the crust and alter strain distribution along the rift. Such modification may support the development and maintenance of the magmatic system beneath the volcano. After removing regional plate motion, we also identify local deformation linked to geothermal activity and post-eruptive lava processes. These findings improve understanding of tectonic–volcanic interactions and provide constraints for deformation monitoring and volcanic hazard assessment in rift zones.

Key Points:

- Global Navigation Satellite System and interferometric synthetic aperture radar data jointly constrain the North American-Eurasian plate divergence across the Krafla volcanic system, Iceland
- Locking depth is shallowest (~2.7 km) beneath the Krafla caldera and increases northward to ~4.9 km and southward to ~6.8 km
- We identify three local areas of deflation from residual velocities, related to geothermal activity and lava subsidence

Supporting Information:

Supporting Information may be found in the online version of this article.

Correspondence to:

Y. Yang,
yiy1@hi.is

Citation:

Yang, Y., Sigmundsson, F., Geirsson, H., Biggs, J., Drouin, V., Sepúlveda-Araya, J., et al. (2026). Plate divergence at the Krafla volcanic system, Iceland: Insight from GNSS geodesy and Sentinel-1 satellite radar interferometry in 2002–2024. *Journal of Geophysical Research: Solid Earth*, *131*, e2026JB034040. https://doi.org/10.1029/2026JB034040

Received 13 FEB 2026
Accepted 4 AUG 2026

Author Contributions:

Conceptualization: Yilin Yang, Freysteinn Sigmundsson, Halldór Geirsson, Juliet Biggs, Taco Broerse
Data curation: Yilin Yang, Josefa Sepúlveda-Araya, Sigrún Hreinsdóttir
Formal analysis: Yilin Yang, Josefa Sepúlveda-Araya

© 2026 The Author(s). Journal of Geophysical Research: Solid Earth published by Wiley Periodicals LLC on behalf of American Geophysical Union. This is an open access article under the terms of the Creative Commons Attribution-NonCommercial License, which permits use, distribution and reproduction in any medium, provided the original work is properly cited and is not used for commercial purposes.

1. Introduction

Improved knowledge of processes at divergent plate boundaries, where oceanic crust forms, is important for the general understanding of tectonics and lithospheric evolution (e.g., Augustin et al., 2021; Smith & Cann, 1993; Toomey et al., 2007). The system of mid-ocean ridges (MOR) is the most common type of divergent plate

Funding acquisition: Freysteinn Sigmundsson, Halldór Geirsson
Investigation: Yilin Yang, Taco Broerse, Sandra Verhagen
Methodology: Yilin Yang, Freysteinn Sigmundsson, Chiara Lanzi
Project administration: Freysteinn Sigmundsson
Resources: Yilin Yang, Sigrún Hreinsdóttir, Chiara Lanzi, Sandra Verhagen
Software: Yilin Yang
Supervision: Freysteinn Sigmundsson, Halldór Geirsson, Juliet Biggs, Vincent Drouin, Joachim Gottsmann
Validation: Yilin Yang, Freysteinn Sigmundsson, Juliet Biggs, Vincent Drouin, Taco Broerse
Visualization: Yilin Yang
Writing – original draft: Yilin Yang
Writing – review & editing: Yilin Yang, Freysteinn Sigmundsson, Halldór Geirsson, Juliet Biggs, Vincent Drouin, Josefa Sepúlveda-Araya, Sigrún Hreinsdóttir, Chiara Lanzi, Joachim Gottsmann, Taco Broerse

boundary and accounts for about 75% of Earth's volcanism (Bennett et al., 2019). However, less than 2% of MOR are above sea level, posing challenges for measuring their deformation and seismicity. Thus, subaerial portions of MOR, such as Iceland and Afar region in Africa (e.g., Pagli et al., 2014; Sigmundsson et al., 2020; Wright et al., 2012), offer good opportunities for measuring plate spreading and volcano-tectonic processes.

The Krafla volcanic system in the Northern Volcanic Zone (NVZ) of Iceland (Figure 1) is well suited for studying plate divergence at the subaerial part of the MOR system, because of the extensive set of geodetic observations available. The system is a segment of the divergent boundary between the Eurasian and North American plates. Global plate motion models give a spreading rate of 16.3–18.6 mm/yr in N283.0°–286.7°E in this area (Argus et al., 2010; DeMets et al., 1994, 2010). The volcanic system consists of a central volcano with a 9 km × 7 km wide caldera and a 4–10 km wide fissure swarm (rift zone), striking NNE–SSW, and extending 40 km to the south and 50 km to the north from the caldera (Figure 1; Hjartardóttir et al., 2012; Lanzi et al., 2023; Opheim & Gudmundsson, 1989; Sæmundsson, 1991). Plate spreading occurs at a relatively small angle from the rift-normal direction, featuring some obliquity. The volcanic system hosts two high-temperature geothermal fields (Krafla and Bjarnarflag; green stars in Figure 1b), which have been exploited since 1960s. The most recent rifting episode at Krafla occurred in 1975–1984, including about 20 rifting events, 9 of which led to eruptions (e.g., Björnsson et al., 1977; Einarsson, 1991; Tryggvason, 1980). The current large-scale deformation at Krafla is dominated by plate spreading and glacial isostatic adjustment (GIA) (e.g., Drouin, Sigmundsson, Ófeigsson, et al., 2017).

Knowledge of background plate spreading deformation enhances our capability to detect, model and interpret small-scale and small-magnitude deformation patterns from magmatic, hydrothermal and rift-related processes at the Krafla volcanic system. These include: (i) a decay in subsidence rate from ∼50 mm/yr during 1989–1992 to ∼3 mm/yr during 2002–2005, associated with a deflating shallow magma body at ∼2.5 km depth beneath Krafla (Sturkell et al., 2008); (ii) geothermal-related ground deformation of less than ∼6 mm/yr horizontally and ∼15 mm/yr vertically, with shallow sources above ∼2.5 km depth (Drouin, Sigmundsson, Verhagen, et al., 2017; Lanzi et al., 2023); and (iii) a regional deformation anomaly of 7.6–9.8 mm/yr in the east component during 2014–2015 across the study area (Yang et al., 2023).

The Krafla volcanic system has abundant geodetic observations for studying plate spreading. Global Navigation Satellite System (GNSS) surveys in the area began in 1986 and the GNSS network now contains over 100 benchmarks. Four continuous GNSS (cGNSS) stations have been operating for more than a decade and two additional stations at the Krafla caldera center were installed in 2019. Since 2010, 78 sites on average have been measured annually during GNSS campaigns. Interferometric analysis of synthetic aperture radar satellite images (InSAR) has also been applied to monitor deformation in the area since 1990s, using multiple satellite missions (e.g., Ali et al., 2014; Cao et al., 2023; Drouin, Sigmundsson, Verhagen, et al., 2017; Metzger & Jónsson, 2014).

There are several existing models of secular, inter-rifting plate boundary deformation at Krafla, considering the change in velocity from one plate to the other and that the two plates are locked together above a certain locking depth during inter-rifting periods. The deeper the locking depth, the wider the plate boundary deformation zone. In volcanic rift settings, locking depth is also often linked to the crustal depth of the brittle-ductile transition (e.g., Drouin, Sigmundsson, Ófeigsson, et al., 2017). Existing plate boundary models therefore aimed to infer plate boundary geometry and locking depth using GNSS observations (Barreto et al., 2025; Drouin, Sigmundsson, Ófeigsson, et al., 2017; Metzger et al., 2013; Árnadóttir et al., 2009), InSAR data (Cao et al., 2023; Drouin & Sigmundsson, 2019), or their combination (Metzger & Jónsson, 2014). Most of these studies simplified the plate boundary across the Krafla volcanic system into two linear segments. However, Metzger & Jónsson (2014) and Drouin, Sigmundsson, Ófeigsson, et al. (2017) showed that locking depth varies significantly at Krafla, ranging at least from ∼3 to 6 km. Such geometric simplifications using long, straight plate boundary segments (Cao et al., 2023; Drouin & Sigmundsson, 2019) can result in inferred plate boundaries that are offset from the Krafla fissure swarm (Hjartardóttir et al., 2012) and inconsistent with the strikes of mapped fractures (Corti et al., 2021), indicating that simplified geometries cannot adequately represent the local stress field. The spatially variable plate boundary profile along the NVZ inferred by Drouin, Sigmundsson, Ófeigsson, et al. (2017) partly addressed this issue but suffered from large uncertainties in locking depth (up to ∼10 km) due to sparse GNSS coverage.

The vast increase in available geodetic data (both GNSS and InSAR) allows us to derive an improved plate boundary model with a more precise description of geometry and locking depths. In earlier studies, Metzger & Jónsson (2014) used 92 interferograms and Drouin, Sigmundsson, Ófeigsson, et al. (2017) included ∼35 GNSS sites from Krafla. Conversely, our current data sets including more than 100 GNSS sites and thousands of SAR

21699356, 2026, 8, Downloaded from https://agupubs.onlinelibrary.wiley.com/doi/10.1029/2026JB034040 by Technical University Delft, Wiley Online Library on [02/09/2026]. See the Terms and Conditions (https://onlinelibrary.wiley.com/terms-and-conditions) on Wiley Online Library for rules of use; OA articles are governed by the applicable Creative Commons License

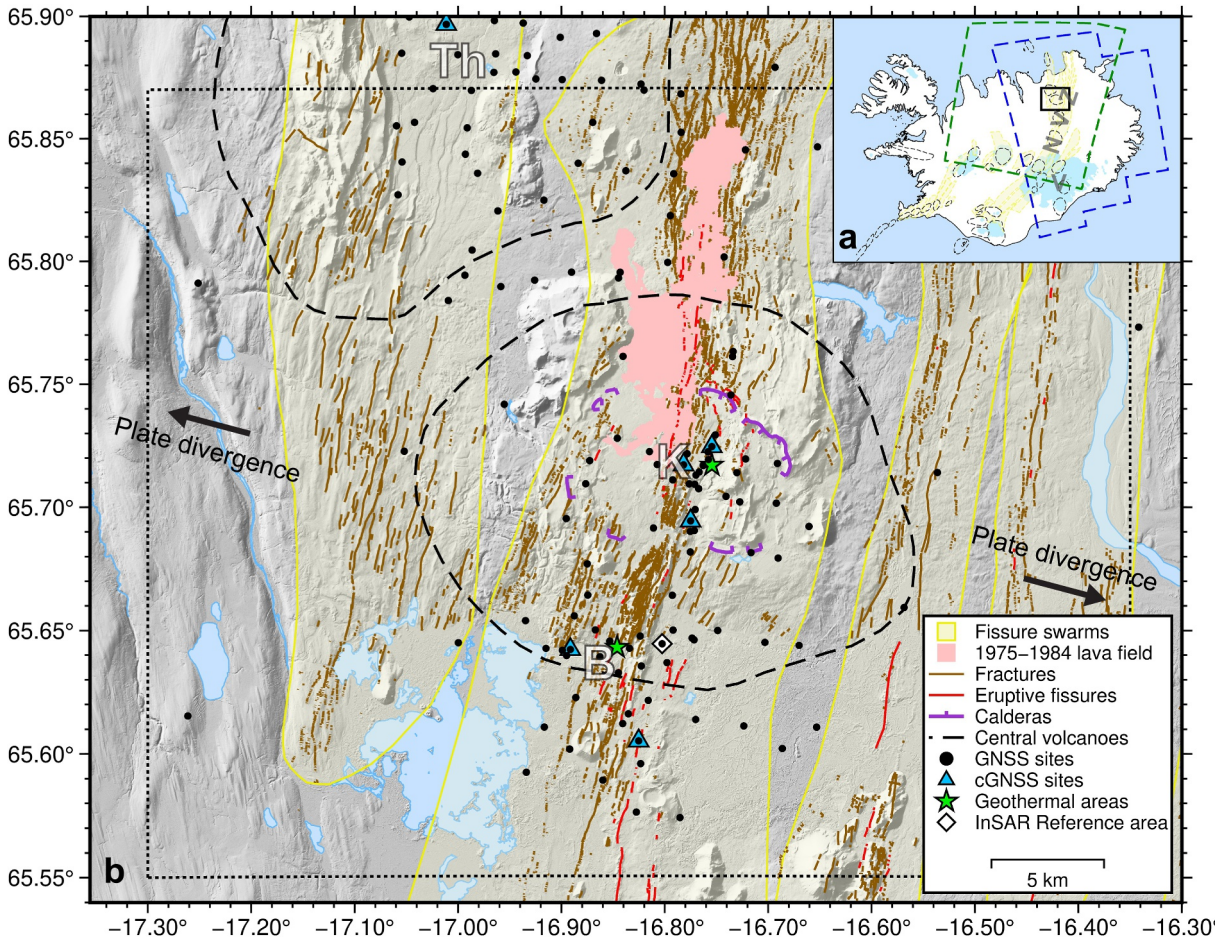

Figure 1. (a) Map of Iceland. The rectangle indicates the study area. The light blue areas indicate glaciers where V indicates Vatnajökull. The green and blue dashes outline the descending and ascending frames of Centre for the Observation and Modelling of Earthquakes, Volcanoes and Tectonics-Looking inside the Continents from Space Sentinel-1 InSAR products, respectively, available in 2024 for the Krafla area. (b) Map of the study area. Th indicates the Þeistareykir (Theistareykir) volcanic system, K indicates the Krafla volcanic system and B indicates the Bjarnarflag geothermal field. The dotted rectangle indicates the area of InSAR deformation analysis. The direction of plate divergence is from DeMets et al. (2010). The topography is from LMÍ (2020), fractures from Hjartardóttir et al. (2015), and fissure swarms, central volcanoes and caldera are from Jóhannesson and Sæmundsson (2009).

interferograms covering the central part of the Krafla volcanic system can provide better constraint on the plate divergence. Integrating these two types of data sets also combines the strengths of the wide spatial coverage from InSAR and three-dimensional displacement measurements from GNSS, leading to more reliable plate boundary models than using only one of them.

In this study, we aim to separate the large-scale plate divergence signal from local deformation patterns, by constraining a plate boundary model using geodetic observations that complies with local stress field and fissure swarm geometries. The model represents the central Krafla volcanic system with six linear segments, of which the geometry is determined by inversion of GNSS and InSAR horizontal velocity fields. We then investigate local deformation using residual horizontal velocity fields and relate these to patterns in the vertical velocity field. Finally, we compare the new plate boundary model with plate motions from global and existing regional models, geological features and seismicity in the area, and discuss how plate divergence interacts with volcanic activities.

2. Data

This study analyzes GNSS data collected during 2002–2024 and Sentinel-1 SAR interferograms in 2015–2023 to derive the long-term velocity field of the area. To correct velocity fields for GIA, which influences ground deformation in a much larger scale than plate boundary locking, we incorporate the GIA deformation model of Iceland by Auriac (2014).

21699356, 2026, 8, Downloaded from https://agupubs.onlinelibrary.wiley.com/doi/10.1029/2026JB034040 by Technical University Delft, Wiley Online Library on [02/09/2026]. See the Terms and Conditions (https://onlinelibrary.wiley.com/terms-and-conditions) on Wiley Online Library for rules of use; OA articles are governed by the applicable Creative Commons License

21699356, 2026, 8, Downloaded from https://agupubs.onlinelibrary.wiley.com/doi/10.1029/2026JB034040 by Technical University Delft, Wiley Online Library on [02/09/2026]. See the Terms and Conditions (https://onlinelibrary.wiley.com/terms-and-conditions) on Wiley Online Library for rules of use; OA articles are governed by the applicable Creative Commons License

2.1. GNSS

We process GNSS data collected at both continuous and campaign sites between 2002 and 2024 at University of Iceland using GAMIT/GLOBK 10.75 to obtain coordinate time series in the ITRF2014 (IGb14) reference frame, using reference stations in Iceland and globally (Altamimi et al., 2016; Herring et al., 2018). The processing uses an elevation mask angle of 10° and IGS14 azimuth and elevation dependent absolute phase center model for all antennas. We use International GNSS Service final orbit products as a priori constraint, and solve for satellite orbits, earth rotation parameters, atmospheric zenith delay (every 2 hr), and three atmospheric gradients per day along with site coordinates. Zenith wet tropospheric delays are derived by scaling slant delays using the Vienna Mapping Function (VMF1; Boehm et al., 2006). Corrections include ocean tidal loading using the FES2004 model (Lyard et al., 2006), solid-Earth and pole tide (Danis et al., 2004). Finally, we convert the derived coordinate time series to topocentric coordinate system (east, north, up) for better representing local deformation (see available campaign GNSS data in Figure S1 in Supporting Information S1 and examples of GNSS time series in Figures S2 and S3 in Supporting Information S1).

Stable GNSS site coordinate time series (i.e., without transient or anomalous deformation signals) can be described as:

$$y = a + bt + \sum_{i=1}^{n}[c_i \sin(2\pi it) + d_i \cos(2\pi it)] + \varepsilon, \quad (1)$$

where y is the coordinate at time t, a represents initial site position, c_i and d_i represent the amplitudes of seasonal signals (Blewitt & Lavallée, 2002) and ε represents the residuals. The linear term, b, represents the long-term site velocity and is here estimated together with other parameters (a, c_i, d_i) using the Weighted Least Square method, with weights derived from the formal uncertainties of the GNSS position estimates (following the same procedures as in Yang et al., 2023). The number of seasonal signals (n) considered in the velocity estimation is set to $n = 2$ for cGNSS sites (annual and semi-annual signals) and $n = 0$ for campaign sites (no seasonal signal), because the periodicities are mitigated at campaign sites by conducting measurements in the same period each year.

Before velocity estimation, we manually inspect the time series and have detected no significant jumps, except at cGNSS site LHNC, where instrument and power failures caused data gaps and jumps. This site is not considered in subsequent analysis. Outliers in cGNSS time series are removed using the inter-quartile range criterion (Nikolaidis, 2002). For campaign GNSS sites, we handle outliers after the velocity estimation (see next paragraph) and during the inversion scheme (Section 3.3), since statistical methods cannot handle sparse time series.

Several studies have identified transient deformation signals at Krafla during the period 2002–2024 (Gudnason et al., 2024; Lanzi et al., 2023; Metzger et al., 2013; Yang et al., 2023). However, these signals usually last less than 2 years with magnitudes below 10 mm/yr in the horizontal components, and their impact on the estimated velocity of the full study period at campaign GNSS sites is generally smaller than 2 mm/yr (see synthetic data experiments in Figure S4 in Supporting Information S1), comparable to the fitting errors (Leonard et al., 2007). To reduce biases from insufficient observations and outliers at campaign sites, we do not consider sites with vertical velocity uncertainties larger than 3 mm/yr, representing approximately the 95% confidence limit of stable stations. Vertical velocities are used for site selection for their larger uncertainties and more sensitivity to noise than horizontal velocities. Finally, we use the Euler pole and rotation rate of the Eurasian plate from ITRF2014 plate motion model to evaluate the expected displacement rate at each site, thereby referencing GNSS horizontal velocity field to the stable Eurasian plate (Altamimi et al., 2017).

GNSS velocity uncertainties are first estimated assuming white noise in the time series and subsequently scaled by an empirical factor of 30. We introduce this scaling because the sparse campaign observations do not allow robust estimation of more complex noise models, whereas GNSS time series are known to contain time-correlated noise (e.g., Williams, 2003; Yang et al., 2023). We evaluate velocity uncertainties at the cGNSS stations using the Hector software (Bos et al., 2013) following the same approach as in Yang et al. (2023). The results suggest that the white-noise assumption underestimates uncertainties by approximately one order of magnitude compared to the approach that includes time-correlated flicker noise (Figure S2 in Supporting Information S1). We combine this order-of-magnitude correction with an additional empirical factor of 3 to account for the sparse data of campaign sites, resulting in the scaling factor of 30. In the inversion, we weight both continuous and campaign GNSS sites using these scaled uncertainties to ensure a consistent treatment of the GNSS data set.

21699356, 2026, 8, Downloaded from https://agupubs.onlinelibrary.wiley.com/doi/10.1029/2026JB034040 by Technical University Delft, Wiley Online Library on [02/09/2026]. See the Terms and Conditions (https://onlinelibrary.wiley.com/terms-and-conditions) on Wiley Online Library for rules of use; OA articles are governed by the applicable Creative Commons License

2.2. InSAR

We conduct a Small Baseline Subset (SBAS) time series analysis using Sentinel-1 radar interferograms from 2015 to 2023 using the Centre for the Observation and Modelling of Earthquakes, Volcanoes and Tectonics (COMET)-Looking inside the Continents from Space (LiCS) system (Lazecký et al., 2020; Morishita et al., 2020). We choose the spatial extent (dotted rectangle in Figure 1b) to capture the spatial variation of the plate spreading deformation in the satellite line-of-sight (LOS) velocity field and to ensure sufficient coverage for constraining the inversion. Interferogram products are generated with the LiCSAR software (Lazecký et al., 2020), and were multilooked by factors of 5 in azimuth and 20 in range to improve the signal-to-noise ratio, achieving a pixel size of ∼100 m × 100 m. The topographic correction is derived using Copernicus Digital Elevation Model at 90 m resolution (ESA, 2020).

We perform time series analysis of 151 interferograms from ascending track T147 and 165 interferograms from descending track T9 using LiCSBAS software (Morishita et al., 2020), which follows the New SBAS approach (e.g., Doin et al., 2011; López-Quiroz et al., 2009). The interferometric network is well connected prior to 2022, including both short temporal baselines (∼3 months) and long baselines (∼1 year) (Figure S5 in Supporting Information S1). The New SBAS approach incorporates a linear deformation constraint and allows the inclusion of interferograms with short temporal baselines after 2022, despite gaps in the spatiotemporal baseline network. Although such gaps may affect the representation of non-linear transient deformation signals, comparisons indicate that they do not significantly bias the estimated long-term velocities (Figure S6 in Supporting Information S1), given the dense and well-connected network before 2022, and the relatively stable long-term deformation in the study area. We correct large-scale atmospheric errors using the Generic Atmospheric Correction Online Service for InSAR (Yu et al., 2018) following Elliott et al. (2025), as the limited spatial coverage of the pre-2019 cGNSS network does not allow constructing a robust local atmospheric model (e.g., Albino et al., 2025). Because the interferograms from early fall to late spring in the study area have low coherence due to snow cover, we only include images acquired between May and late September to maximize the use of high-quality interferograms.

We use the nearest pixel of benchmark FM15 (white diamond in Figure 1b) as the reference of the InSAR LOS velocity fields (Figure S7 in Supporting Information S1), where GNSS time series shows minimal vertical displacement. This benchmark has also served as the reference point for leveling measurements over decades (Sturkell et al., 2008). Assuming that the displacement in north component has a negligible contribution to LOS velocities, we decompose the LOS velocities into approximate estimates of eastward (near-east) and vertical (near-up) components (Motagh et al., 2017; Wright et al., 2004). We reference InSAR near-east and near-up velocity fields to the stable Eurasian plate by subtracting the median difference between InSAR and GNSS velocities (10.6 and 1.6 mm/yr for the near-east and near-up components, respectively).

To reduce the computational cost of inversion, we down-sample the near-east InSAR velocity map uniformly from a pixel size of ∼100 m × 100 m to ∼600 m × 1000 m, resulting in 2,464 pixels. The smaller pixel size in the X-direction (Easting) helps preserve deformation variations across the plate boundary deformation zone. All data point coordinates are projected into a local Cartesian coordinate system (X, Y).

We represent InSAR velocity uncertainties using a semivariogram function to account for spatial correlated errors (Bagnardi & Hooper, 2018). The semivariogram parameters for the near-east velocities are estimated after preliminarily correcting for plate boundary deformation based on a priori information from previous models (e.g., Drouin, Sigmundsson, Ófeigsson, et al., 2017). This fitted semivariogram suggests that InSAR velocities are correlated over distance of ∼2.4 km before reaching a stable variance level corresponding to a standard deviation of ∼0.8 mm/yr, together with a small zero-lag-distance noise component of ∼0.1 mm/yr (Figure S8 in Supporting Information S1).

2.3. Deformation From Glacial Isostatic Adjustment

GIA deformation due to retreat of Icelandic ice caps since 1890 affects ground deformation throughout Iceland. To remove its imprint in the observed velocity fields, we use the velocities predicted by the model developed by Auriac (2014). It is a numerical model using a finite element method, with two elastic layers overlying a viscoelastic half-space. The upper elastic layer is 1 km thick, with a Young's modulus (E) of 14 GPa and a Poisson's ratio (ν) of 0.17. The lower elastic layer and the viscoelastic half-space share the same elastic properties,

21699356, 2026, 8, Downloaded from https://agupubs.onlinelibrary.wiley.com/doi/10.1029/2026JB034040 by Technical University Delft, Wiley Online Library on [02/09/2026]. See the Terms and Conditions (https://onlinelibrary.wiley.com/terms-and-conditions) on Wiley Online Library for rules of use; OA articles are governed by the applicable Creative Commons License

$E = 74$ GPa and $\nu = 0.25$. The model calculates deformation based on an ice thinning model for 1890–2010. Auriac (2014) inverted for the thickness of the lower elastic layer and the viscosity (η) of the viscoelastic half-space by using GNSS and InSAR velocity fields from 1993 to 2004, inferred to be 21 km thick and $\eta = 8.4 \times 10^{18}$ Pa s, respectively.

Although this time-varying model predicts GIA deformation velocities in 2008–2010, it is constrained with data spanning 1993–2004 and the model does not account for the variable and accelerated glacier retreat in recent years (The GlaMBIE Team, 2025). The model tends to underestimate GIA signals in observed velocity fields after 2004. To preserve the spatial deformation pattern while increasing the predicted velocities in line with observations, we follow the same approach as several previous studies (Drouin & Sigmundsson, 2019; Drouin, Sigmundsson, Ófeigsson, et al., 2017; Li et al., 2022). This approach estimates scaling factors for the Auriac (2014) model outputs for the 2008–2010 period and we then subtract the scaled outputs from our observed velocity fields. Drouin, Sigmundsson, Ófeigsson, et al. (2017) found that the misfit between modeled and observed GIA deformation differs for the horizontal and vertical components in north Iceland when using a single scaling factor. We therefore apply separate scaling factors for the horizontal and vertical velocities, following Drouin, Sigmundsson, Ófeigsson, et al. (2017).

3. Methods

We model horizontal deformation resulting from the plate boundary locking using a kinematic model and estimate model parameters through a Bayesian inversion framework. Section 3.1 and 3.2 describe the kinematic model and the Bayesian inversion framework, respectively. Section 3.3 details the inversion strategy. At divergent plate boundaries, upwelling mantle is likely to have an important contribution to vertical velocities so the kinematic model we use here is not well suited to replicate vertical displacements. Therefore, we analyze vertical velocity fields independently and do not include them in the plate boundary inversion. Instead, we correct the vertical velocities for GIA deformation and the regional subsidence due to rheological anomalies undergoing extension (Section 3.4) and then use them qualitatively to interpret local deformation patterns in combination with the horizontal residual velocities.

3.1. Kinematic Modeling of Plate Boundary Deformation

We describe the plate boundary deformation using the kinematic back slip model (Metzger et al., 2011; Savage, 1983), which has been applied to north Iceland (Ali et al., 2014; Barreto et al., 2025; Drouin & Sigmundsson, 2019; Metzger & Jónsson, 2014). The model assumes that two tectonic blocks are locked from the surface to a certain depth and move freely below. To simulate free plate motion at depth, the model assigns half spreading rate on each side of the plate boundary axis (Figure 2a). Then, to simulate the locking at shallow crust along the plate boundary axis, we superimpose the deformation field produced by an infinitely long vertical plane dislocation from the surface to the locking depth with the opposite movements, assuming a uniform elastic half-space (namely the back slip in Figure 2b; Okada, 1985). For oblique plate spreading with some obliquity, the back slip dislocation includes both strike-perpendicular (closing) and strike-parallel (shear) components, applied in the opposite direction of the plate motion at the same magnitude. These back slip components are directly related to the magnitude of the free plate motion rate (u) using the obliquity angle (α) between the plate spreading direction and plate boundary strike:

$$u_{\text{closing}} = -u \sin \alpha, \qquad u_{\text{shear}} = -u \cos \alpha, \tag{2}$$

where u_{closing} and u_{shear} represent the closing and shear components of the back slip dislocation, respectively (with opening and right-lateral defined as positive). Figure 2d shows an example deformation profile predicted by the back slip model.

In this study, we approximate an infinitely long dislocation plane by setting its length to 10 times the physical segment length. We evaluate deformation locally by assigning each observation point to a single plate boundary segment. For each point, we construct a line parallel to the spreading direction and calculate its intersection with the plate boundary axis. We then assign the observation point to the segment of which the finite length contains this intersection (Figure 2). This approach allows deformation parameters to be resolved independently at each

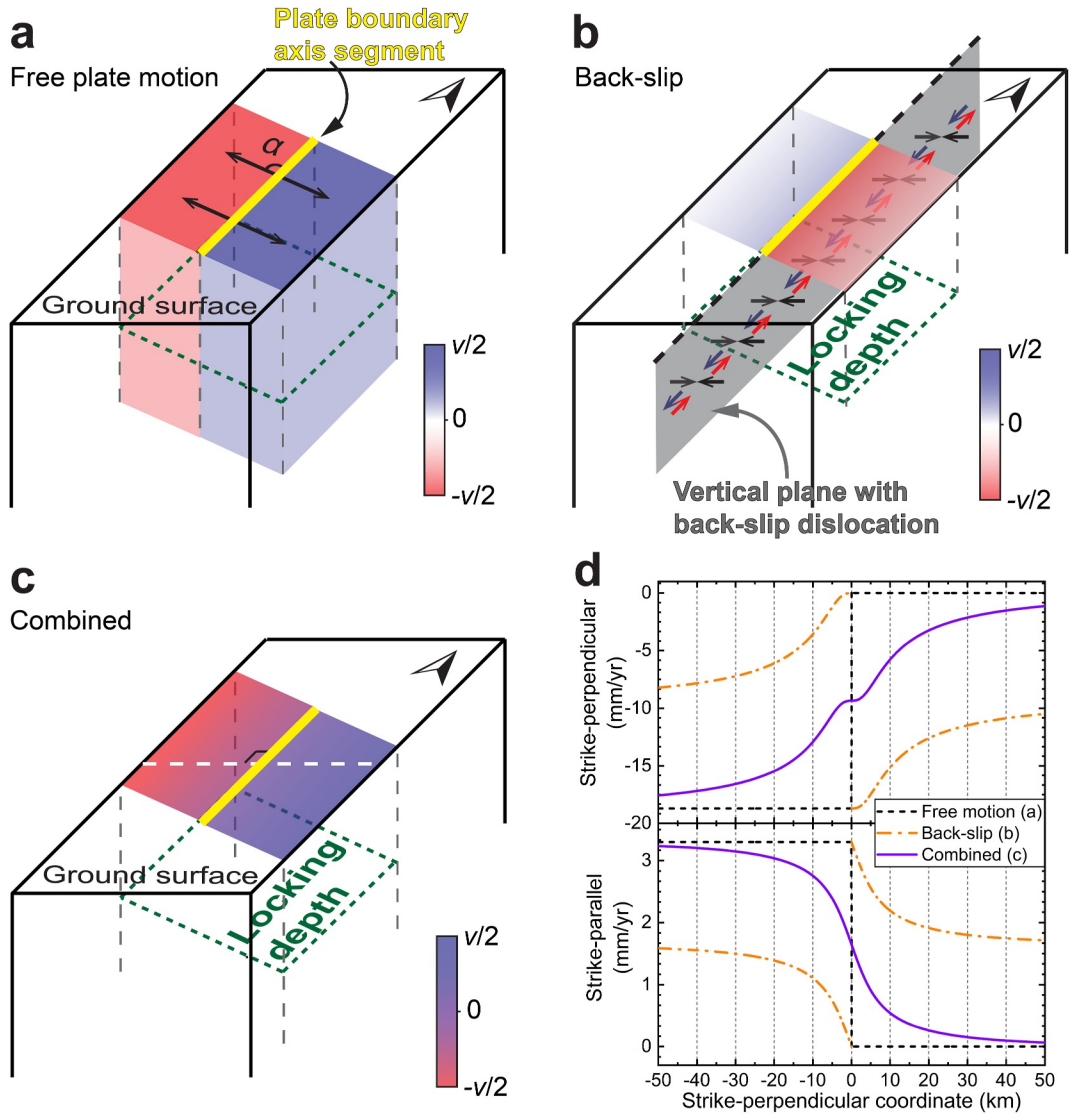

Figure 2. Illustration of the back slip model at a segment of the plate boundary axis. (a) Kinematic representation of free plate motion by assigning half spreading rate on each side of the plate boundary axis. The colormap indicates the velocity perpendicular to the plate boundary axis. α represents the obliquity of spreading. (b) Kinematic representation of the plate boundary locking by superimposing the deformation generated by back slip dislocation plane. The dark gray arrows indicate the strike-perpendicular component (closing). The red and blue arrows indicate the strike-parallel component (shear). Although the back slip dislocation is implemented as an infinitely long plane, deformation is evaluated locally, such that each segment dominates deformation within its domain along the plate spreading direction. (c) Velocity fields predicted by a back slip model combining panels (a) and (b). The white dashed line is perpendicular to the yellow line and indicates the profile in panel (d). (d) Example velocity profiles of the back slip model. The full spreading rate is in this example 19 mm/yr with $\alpha = 80°$. The locking depth is set to 6 km. We reference the velocities to the right-hand plate by subtracting half of the spreading rate in the spreading direction.

segment. To ensure a consistent reference frame in the inversion, we also reference the modeled velocities to the stable Eurasian plate by subtracting half of the spreading rate in the spreading direction.

3.2. Bayesian Inversion Framework

Given the nonlinearity of the back slip model problem and the trade-off among parameters, we apply a Bayesian inversion scheme to establish the plate boundary model. With a nonlinear model function (**G**) with its parameters (**m**), the observations (**v**) can be written as:

21693356, 2026, 8, Downloaded from https://agupubs.onlinelibrary.wiley.com/doi/10.1029/2026JB034040 by Technical University Delft, Wiley Online Library on [02/09/2026]. See the Terms and Conditions (https://onlinelibrary.wiley.com/terms-and-conditions) on Wiley Online Library for rules of use; OA articles are governed by the applicable Creative Commons License

$$\mathbf{v} = \mathbf{G}(\mathbf{m}) + \boldsymbol{\epsilon}, \tag{3}$$

where $\boldsymbol{\epsilon}$ represents errors. Here, $\mathbf{v}$ is the vector of geodetic observations. Bayesian inversion calculates the probability of each parameter $\mathbf{m}$ given the data, $p(\mathbf{m}|\mathbf{v})$, which according to Bayes theorem can be written as:

$$p(\mathbf{m}|\mathbf{v}) = \frac{p(\mathbf{v}|\mathbf{m})\,p(\mathbf{m})}{p(\mathbf{v})}, \tag{4}$$

where $p(\mathbf{m})$ is the prior probability of parameter values, usually assumed to conform to a joint uniform distribution within their bounds (Jeffreys, 1939; Ulrych et al., 2001). Given a sample of model parameters $\mathbf{m}$, and assuming that the errors conform to a multivariate Gaussian distribution, a likelihood function evaluating the probability of the geodetic observations $\mathbf{v}$, $p(\mathbf{v}|\mathbf{m})$ can be calculated:

$$p(\mathbf{v}|\mathbf{m}) = (2\pi)^{-N/2}|\boldsymbol{\Sigma}_{\mathbf{v}}|^{-\frac{1}{2}} \times \exp\left[-\frac{1}{2}(\mathbf{v}-\mathbf{G}(\mathbf{m}))^{\mathrm{T}}\boldsymbol{\Sigma}_{\mathbf{v}}{}^{-1}(\mathbf{v}-\mathbf{G}(\mathbf{m}))\right], \tag{5}$$

where N is the number of observations and $\boldsymbol{\Sigma}_{\mathbf{v}}$ is the covariance matrix of the observations $\mathbf{v}$. The marginal probability of the observations $p(\mathbf{v})$ is a constant to normalize the posterior probability distribution. A specific iterative sampling can achieve an estimate of a posterior joint probability density function (PDF) of unknown parameters $\mathbf{m}$, providing all their statistics. For instance, estimates can be derived from the mean, median, maximum probability, and 95% confidence intervals of the marginal posterior PDF for each parameter.

The sampling method is crucial for the estimation of $p(\mathbf{m}|\mathbf{v})$. We follow the framework proposed by Bagnardi and Hooper (2018) by modifying the Geodetic Bayesian Inversion Software (GBIS) in MATLAB®. This framework iteratively samples on the unknown parameters $\mathbf{m}$ using Markov chain Monte Carlo (MCMC) method with the Metropolis–Hastings algorithm and automatic step size selection. The method is flexible to modify for different scenarios (e.g., Yang et al., 2023). We assess the convergence of an inversion from the stability of the posterior distributions and the variation of the Markov chain. A chain is considered converged based on visual inspection, when the sampled parameters show stable mean values and variability without systematic drift over the sampling iterations. Otherwise, the inversion fails to converge, which can be caused by model non-uniqueness, weak data constraints, or inappropriate priories or step sizes.

3.3. Inversion Strategies

GNSS horizontal velocities and InSAR near-east velocities jointly constrain the plate boundary model. We divide the plate boundary axis into multiple segments and use a two-step inversion scheme to reduce model non-uniqueness. The first-step inversion aims to infer the location and geometry of the plate boundary. To ensure continuity of the plate boundary axis, adjacent segments are connected through shared nodes, with each segment anchored to the endpoint of the previous one. Accordingly, we invert only for the X-coordinate (easting) at one endpoint of an initial central segment in a local Cartesian system and calculate the other from the inferred strike and prescribed segment length. The geometry of the remaining segments is then determined sequentially from their fixed connecting nodes, segment lengths, and inferred strikes. Here the initial segment is 3 km long and covers the southern half of the Krafla caldera. Segment lengths are initially set to 3 km along the Y-direction (northing) and increased by 1 km if the inversion fails to converge due to weak data constraints. This approach determines six segments across the study area, with lengths ranging from 3 to 9 km along Y-direction, depending on local data quality and spatial coverage (Figure 3b).

In addition to the plate boundary geometry, the first-step inversion jointly estimates kinematic parameters for each segment, including the locking depth, plate spreading rate and direction, together with two individual GIA scaling factors for GNSS and InSAR velocities, using only the data points assigned to the segment (Figure 2c and Section 3.1). Our inversion allows potential local spreading obliquity by estimating the strike and spreading direction as two individual parameters, rather than assuming the plate boundary axis to be perpendicular to the spreading direction a priori.

21699356, 2026, 8, Downloaded from https://agupubs.onlinelibrary.wiley.com/doi/10.1029/2026JB034040 by Technical University Delft, Wiley Online Library on [02/09/2026]. See the Terms and Conditions (https://onlinelibrary.wiley.com/terms-and-conditions) on Wiley Online Library for rules of use; OA articles are governed by the applicable Creative Commons License

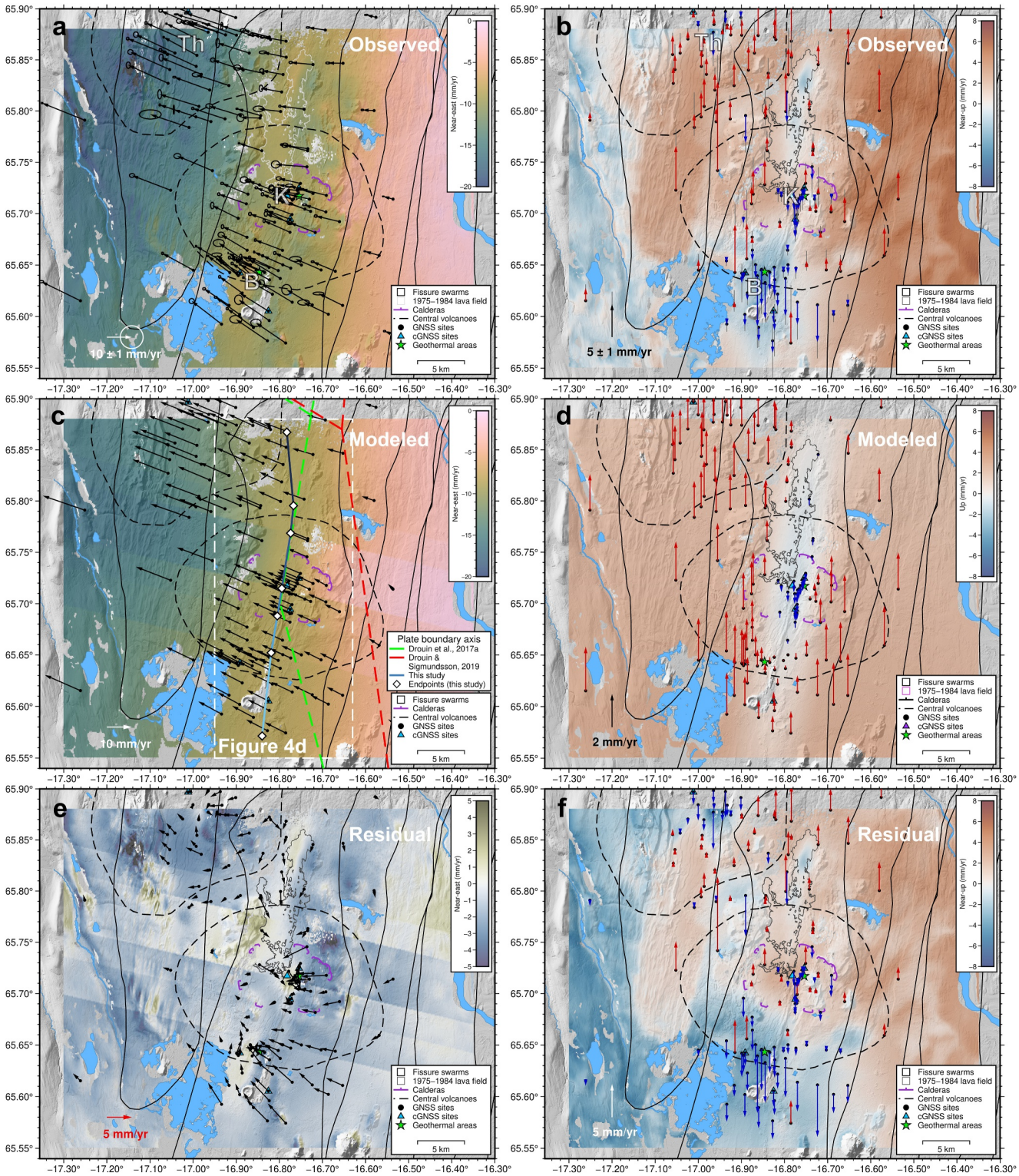

Figure 3. Observed, modeled, and residual long-term velocity fields in the central Krafla volcanic system from Global Navigation Satellite System (GNSS) (2002–2024) and InSAR (2015–2023). (a, b) Observed horizontal (a) and vertical (b) velocity fields. Color maps show InSAR velocity fields. Black arrows show GNSS horizontal velocities with ellipses indicating uncertainties (95% confidence). Blue and red arrows show uplift and subsidence of GNSS vertical velocities, respectively, with their uncertainties (95% confidence) indicated with gray lines centered symmetrically at the arrow tips. Half of a gray line may be covered by the arrow body due to overlap. Th indicates the Þeistareykir (Theistareykir) volcanic system, K indicates the Krafla volcanic system and B indicates the Bjarnarflag geothermal field. (c, d) Modeled horizontal (c) and vertical (d) velocity fields. (e, f) Residual horizontal (e) and vertical (f) velocity fields.

21699356, 2026, 8, Downloaded from https://agupubs.onlinelibrary.wiley.com/doi/10.1029/2026JB034040 by Technical University Delft, Wiley Online Library on [02/09/2026]. See the Terms and Conditions (https://onlinelibrary.wiley.com/terms-and-conditions) on Wiley Online Library for rules of use; OA articles are governed by the applicable Creative Commons License

21699356, 2026, 8, Downloaded from https://agupubs.onlinelibrary.wiley.com/doi/10.1029/2026JB034040 by Technical University Delft, Wiley Online Library on [02/09/2026]. See the Terms and Conditions (https://onlinelibrary.wiley.com/terms-and-conditions) on Wiley Online Library for rules of use; OA articles are governed by the applicable Creative Commons License

Now the plate boundary geometry is fixed, the second-step inversion estimates a uniform spreading rate, spreading direction, and GIA scaling factor for the entire study area, while allowing segment-specific locking depths. This approach avoids inconsistency in plate spreading and discontinuities in the GIA deformation field that could arise from segment-wise estimates. We estimate a single GIA scaling factor for both GNSS and InSAR, even though the data periods are not the same, because separate estimations for each data set leads to unrealistic differences in the InSAR-derived estimates across segments. Although all the segments are jointly inverted in the second-step inversion, the model deformation field of each segment is calculated individually and only applied within its spatial extent along the spreading direction (Figure 2c). That is, each observation is always explained by model prediction of one single segment.

Weighting is applied to balance the contributions of InSAR and GNSS data sets, and the north and east components, on the derived values for the model parameters. Since north-component deformation is constrained only by GNSS velocities (~100 sites in total), whereas both GNSS and InSAR (>2,400 pixels) data constrain the east-component deformation, the east component will dominate the likelihood function. To compensate, we up-weight GNSS velocities in north component by a factor κ_1, defined as:

$$\kappa_1 = \frac{N^{e}_{GNSS} + N^{e}_{InSAR}}{N^{n}_{GNSS}}, \tag{6}$$

where N denotes the number of observations with superscripts and subscripts indicating the components and data sets, respectively. This factor varies between 10 and 40 across sampling iterations of MCMC and between the two inversion steps, for example, $\kappa_1 = 13.5$ for the second-step inversion with 2,464 InSAR pixels and 183 GNSS sites. To ensure comparable overall contributions from InSAR and GNSS to the likelihood function after this adjustment, we further scale the weight of InSAR near-east velocities by an empirical factor κ_2 ($\kappa_2 = 12$ in this study). Unlike κ_1, we do not derive κ_2 analytically but introduce it to balance the relative influence of the InSAR and GNSS data sets in the inversion. Accordingly, the covariance matrix $\mathbf{\Sigma_d}$ can be written as:

$$\mathbf{\Sigma_v} = \begin{pmatrix} \frac{1}{\kappa_1}\mathrm{diag}\left[(\boldsymbol{\sigma}^{n}_{GNSS})^2\right] & 0 & 0 \\ 0 & \mathrm{diag}\left[(\boldsymbol{\sigma}^{e}_{GNSS})^2\right] & 0 \\ 0 & 0 & \frac{1}{\kappa_2}(\mathbf{C}^{e}_{InSAR})^2 \end{pmatrix}, \tag{7}$$

where $\boldsymbol{\sigma}^{n}_{GNSS}$ and $\boldsymbol{\sigma}^{e}_{GNSS}$ represent GNSS velocity uncertainties in north and east components, respectively, $\mathbf{C}^{e}_{InSAR}$ represents the InSAR covariance calculated from the fitted semivariogram function, and diag( ) indicates diagonal matrices.

To further minimize the influence of local deformation and ensure a robust estimation, we apply targeted data filtering and exclusion to tackle the following challenges: (i) InSAR velocities may be affected by topography-related errors due to residual atmospheric artifacts (Albino et al., 2020); (ii) campaign GNSS velocities may be biased by low-quality or sparse observations; and (iii) up-weighting north-component GNSS velocities can amplify the impact of (ii) and local deformation. We apply outlier removal at each sampling iteration of the MCMC method using a Median Absolute Deviation criterion with a 95% confidence threshold (Wilcox, 2005), based on the residuals within each data set. We exclude GNSS sites within 2.5 km of the plate boundary from the inversion if their residuals exceed 1.3 mm/yr in the initial iteration using a priori parameters. For the first-step inversion, we further exclude sites in the Þeistareykir volcanic system (Figure 1) to avoid bias in plate boundary geometry but reintroduce them in the second-step inversion once the plate boundary axis is fixed.

To obtain the posterior PDFs, we run 100,000 sampling iterations in the Bayesian inversion. We adjust parameter search bounds and initial values according to a priori knowledge of the plate boundary and through multiple inversion trials (see Tables S1 and S2 in Supporting Information S1). Visual inspection of the Markov chain suggests the first 30,000 iterations can be considered as burn-in, where the Markov chain has not converged to the target posterior distribution, and the PDFs do not include these iterations.

21699356, 2026, 8, Downloaded from https://agupubs.onlinelibrary.wiley.com/doi/10.1029/2026JB034040 by Technical University Delft, Wiley Online Library on [02/09/2026]. See the Terms and Conditions (https://onlinelibrary.wiley.com/terms-and-conditions) on Wiley Online Library for rules of use; OA articles are governed by the applicable Creative Commons License

3.4. Corrections of the Vertical Velocity Fields

The observed vertical velocities provide qualitative constraints for interpreting residual horizontal deformation. We correct them for long-wavelength signals associated with GIA and plate spreading.

3.4.1. GIA

We estimate the GIA scaling factor for the vertical component using Weighted Least Square method. To reduce the effects of rift-related deformation, we exclude data within 16.95°–16.65°W. Observations are weighted by their velocity uncertainties.

3.4.2. Regional Subsidence Due To Rheological Anomalies Undergoing Extension

Rheological anomalies within the subvolcanic crustal structure, altered by magma and hot rock, can influence the deformation styles (e.g., Dragoni & Magnanensi, 1989; Head et al., 2021). Along a spreading plate boundary, such anomalies can respond to crustal extension by strain localization, causing subsidence in volcanic systems (Lanzi et al., 2024). To account for this effect, we incorporate the finite element model of Lanzi et al. (2024) to represent regional subsidence in the vertical deformation field.

The model is implemented using COMSOL Multiphysics 6.1® (COMSOL, 2022) and consists of a regional 7-km-thick elastic upper crust ($E = 30$ GPa) overlying a viscoelastic half-space ($E = 60$ GPa; $\eta = 5 \times 10^{18}$ Pa s). Three key rheological heterogeneities are implemented (Figure S9 in Supporting Information S1): (i) a low-modulus elastic volume ($E = 7$ GPa) representing caldera infill, tapering from a 9 km × 7 km area at the surface to 6 km × 6 km at 2 km depth, (ii) a viscoelastic up-doming volume beneath the caldera ($E = 30$ GPa; $\eta = 5 \times 10^{18}$ Pa s), extending from 9 km × 9 km at 7 km depth to 6 km × 6 km at 2 km depth, and (iii) a 9-km-wide zone representing the Krafla fissure swarm, extending 50 km north and 40 km south of the caldera, where the elastic-viscoelastic interface ramps from 2 to 7 km depth along strike.

We applied a uniform extension rate of 19.2 mm/yr (the median estimate from Section 4.2) across the model domain. Instead of imposing an upward boundary velocity at the bottom of the model as in Lanzi et al. (2024), we apply a constant vertical shift to the modeled vertical velocities after resampling them onto the InSAR pixel grid and GNSS site locations. The shift is defined as the average difference between the predicted and InSAR-derived vertical velocities at the four corner pixels of the study area (28.7 mm/yr). This shift allows a direct comparison between the model and observations.

4. Results

Figure 3 shows the observed, modeled and residual velocity fields derived from InSAR and GNSS. We first analyze the long-term deformation velocity fields in Section 4.1. Section 4.2 describes the inferred plate boundary model for the central Krafla volcanic system and the corrections for vertical velocities. Section 4.3 focuses on the residual deformation patterns.

4.1. Long-Term Deformation Velocity Fields at Krafla

Both GNSS horizontal and InSAR near-east velocity fields (Figure 3a) reveal a clear extensional deformation pattern across the Krafla volcanic system. Velocities referenced to the stable Eurasian plate increase from near zero in the eastern part of the study area to more than 17 mm/yr in the west. In addition, GNSS horizontal velocity vectors indicate stronger northward motion south of the Krafla central volcano (6–10 mm/yr) than elsewhere (<6 mm/yr).

Observed GNSS vertical velocities (Figure 3b) show overall uplift across the study area, contrasted with millimeter-level yearly subsidence in the Bjarnarflag area and the Krafla caldera center. The fastest uplift in GNSS velocities occurs northwest and east of the Krafla central volcano, reaching up to ∼5 mm/yr. The InSAR near-up velocity field (color map in Figure 3b) is consistent with the GNSS deformation pattern, but suggests two additional areas of uplift, within the Þeistareykir fissure swarm (∼3 mm/yr) and east of the Krafla fissure swarm (5–6 mm/yr). The westernmost part of the study area shows minor vertical deformation (within ±1 mm/yr) from both GNSS and InSAR data.

21699356, 2026, 8, Downloaded from https://agupubs.onlinelibrary.wiley.com/doi/10.1029/2026JB034040 by Technical University Delft, Wiley Online Library on [02/09/2026]. See the Terms and Conditions (https://onlinelibrary.wiley.com/terms-and-conditions) on Wiley Online Library for rules of use; OA articles are governed by the applicable Creative Commons License

We also extract the InSAR velocities from pixels nearest to GNSS sites. The comparison demonstrates good agreement between the InSAR-derived and corresponding GNSS velocities (Figure S10 in Supporting Information S1). To summarize, both GNSS horizontal and InSAR near-east velocity fields effectively capture the plate boundary deformation. Their general consistency suggests relatively stable long-term deformation at Krafla and supports the use of both data sets in a joint inversion of the plate boundary model.

4.2. Plate Boundary Model and Vertical Velocity Corrections at Krafla

Figure 3c shows the modeled horizontal velocity fields using the back slip model and the scaled GIA model predictions, which reproduces the deformation gradient across the Krafla fissure swarm in Figure 3a. Figure 4a shows a zoomed-in view of the inferred plate boundary axis, represented by a segmented line with a color gradient from light to dark blue (south to north). We denote the segments as S1–S6 from south to north. Table 1 and Figures 4d–4f show the median estimates and 95% confidence interval of model parameters. Two strike changes of the inferred plate boundary axis are notable: one from S1 to S2–S4, where the strike increases from a value below N6.5°E to about N9°E; and the other between S5 and S6, where the strike rotates from NE-SW to NW-SE by 5.3°–18.1° to the west north of the Krafla central volcano. The locking depth of the plate boundary axis exhibits significant variation, illustrating an asymmetric deepening trend of locking depth laterally away from the caldera along the south–north direction (discussed in Section 5.5). The marginal PDFs of all model parameters are shown in Figures S11 and S12 in Supporting Information S1. Table S3 in Supporting Information S1 displays the coordinates of the inferred plate boundary axis.

Figure 4g compares the observed and modeled deformation velocities along the spreading direction for all six segments. For the east component, the model fits the observations well and reproduces specifically the flattened velocity gradient near the plate boundary axis (also in Figure 2d). For the north component, segment S3 and S4 show the best fit qualitatively, while other segments show systematic misfits: the model overestimates northward motions in northern segments (S5–S6), while it underestimates northward motions in southern segments (S1–S2). This pattern is further analyzed with the residual velocities in Section 4.3 and discussed in Section 5.6. The estimated GIA correction is spatially similar throughout the study area and its magnitude is small: ∼2 mm/yr in the north component and <1 mm/yr in the east component (Figure S13 in Supporting Information S1).

Figure 3d shows the modeled vertical velocities combining the scaled vertical GIA predictions and the numerical model of regional deformation due to rheological anomalies undergoing extension. The estimation yields a vertical GIA scaling factor of 0.60. The modeled velocity field features a broad uplift of ∼2 mm/yr across most of the study area, and regional subsidence of ∼1 mm/yr at the Krafla caldera. This subsidence reflects the weak caldera infill and shallow elastic-viscoelastic interface in the subvolcanic crust. Figure S14 in Supporting Information S1 shows the scaled vertical GIA predictions and regional subsidence separately.

4.3. Residual Velocity Fields

Generally, both horizontal (Figure 3e) and vertical (Figure 3f) residual velocities are small, especially north of ∼65.65°N where they remain within ±2 mm/yr. Nevertheless, several local and regional deformation patterns stand out in the residuals, as highlighted in Figure 5. Across the Krafla fissure swarm, GNSS residual vectors (Figure 5a) south of the Krafla central volcano (latitudes <65.70°N) generally point northward, with an average residual of 1.5 mm/yr in the north component. In contrast, residual vectors north of the central volcano (latitudes >65.70°N) point southward, with an average north-component residual of −0.7 mm/yr. These observations are consistent with Figure 4g. Therefore, the residual deformation mainly reflects north–south shortening of the fissure swarm centered on the central volcano. Additionally, in the southeastern part of the study area (dashed rectangle 2 in Figures 5a and 5b), GNSS horizontal residual velocities show northwestward motion, with an average magnitude of 3.3 mm/yr and a maximum of 5.9 mm/yr. GNSS vertical residual velocities in the same area mostly indicate subsidence, with an average of −2.3 mm/yr and a minimum of −8.2 mm/yr. InSAR residuals show a similar pattern, but with smaller magnitudes than the GNSS residuals.

Figure 5 also highlights three local deflation areas (dashed rectangle 1 and solid rectangles). In these areas, GNSS horizontal residual vectors point inward, while InSAR near-east residuals show eastward motion on the western side (green colors) and westward motion in the eastern side (blue colors). GNSS vertical residuals indicate subsidence and InSAR residuals show negative deviations from the surrounding residual field in these areas. One of these deflation signals (dashed rectangle 1 in Figure 5) is located at the northernmost part of the lava field

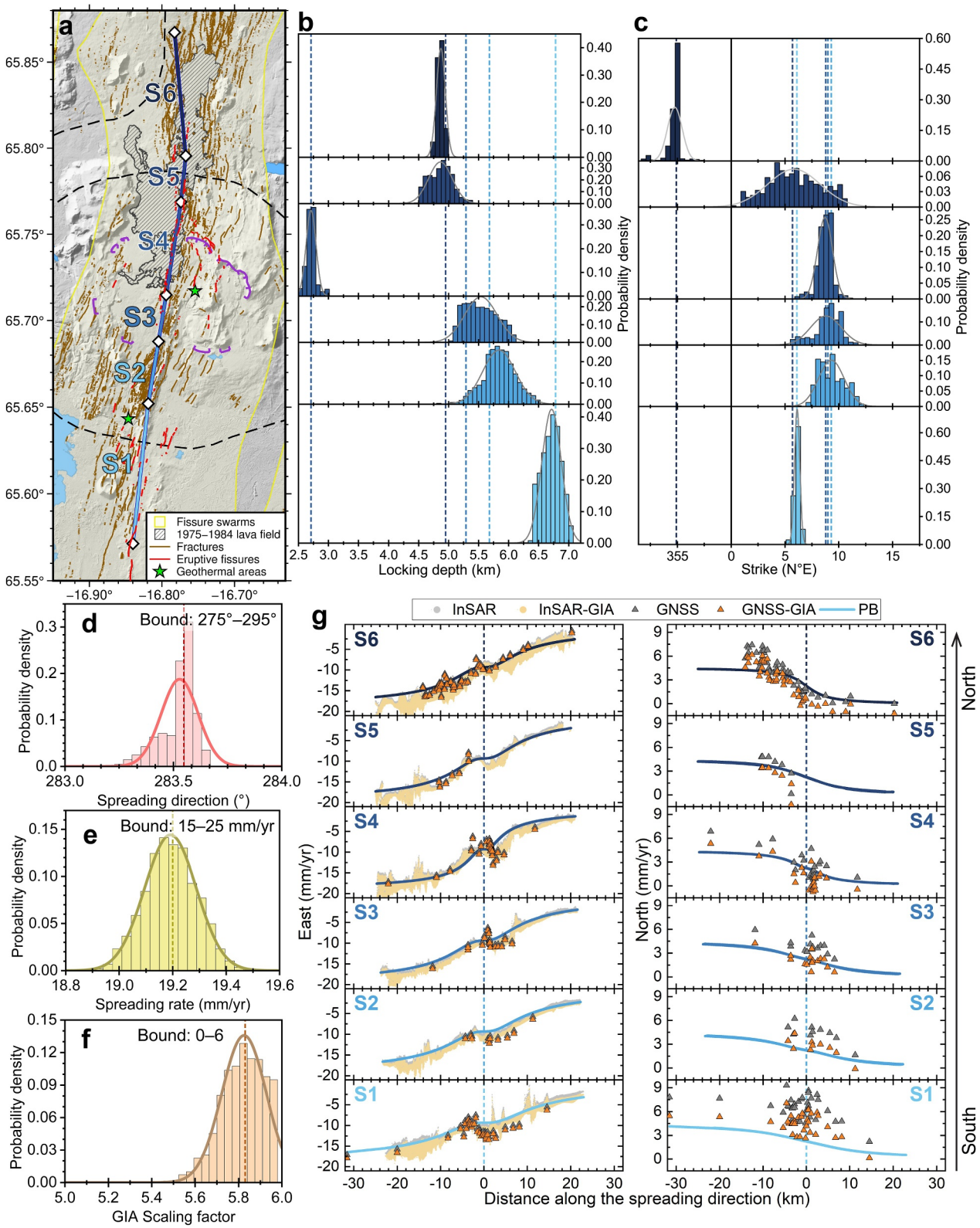

Figure 4.

21699356, 2026, 8, Downloaded from https://agupubs.onlinelibrary.wiley.com/doi/10.1029/2026JB034040 by Technical University Delft, Wiley Online Library on [02/09/2026]. See the Terms and Conditions (https://onlinelibrary.wiley.com/terms-and-conditions) on Wiley Online Library for rules of use; OA articles are governed by the applicable Creative Commons License

21699356, 2026, 8, Downloaded from https://agupubs.onlinelibrary.wiley.com/doi/10.1029/2026JB034040 by Technical University Delft, Wiley Online Library on [02/09/2026]. See the Terms and Conditions (https://onlinelibrary.wiley.com/terms-and-conditions) on Wiley Online Library for rules of use; OA articles are governed by the applicable Creative Commons License

Table 1
Inferred Plate Boundary Model Across the Central Part of the Krafla Volcanic System

Segment	Length in *Y*-axis (km)	Strike	*X*-coordinate of the southern endpoint (km)	Locking depth (km)
S6	8	$N354.9^{+1.0}_{-2.7}°E$	/	$4.86^{+0.20}_{-0.10}$
S5	3	$N5.7^{+4.6}_{-4.5}°E$	/	$4.95^{+0.21}_{-0.42}$
S4	6	$N8.8^{+1.2}_{-2.0}°E$	/	$2.71^{+0.24}_{-0.16}$
S3	3	$N9.0^{+1.8}_{-3.8}°E$	$1.17^{+0.25}_{-0.60}$	$5.29^{+0.35}_{-0.34}$
S2	4	$N9.3^{+0.7}_{-1.6}°E$	/	$5.68^{+0.43}_{-0.50}$
S1	9	$N6.1^{+0.4}_{-0.6}°E$	/	$6.79^{+0.27}_{-0.26}$

Parameters	Estimate
Spreading direction	$N283.5^{+0.2}_{-0.2}°E$
Spreading rate (mm/yr)	$19.2^{+0.2}_{-0.2}$
GIA scaling factor–GNSS and InSAR	$5.83^{+0.16}_{-0.22}$

Note. Parameter estimates are given as the medians of the marginal posterior probability density functions (PDFs), with formal uncertainties derived from their corresponding 95% confidence intervals. The local Cartesian coordinate system is referenced to 65.67°N, 16.83°W. The southern endpoint of segment S3 is inferred from the inversion, while its northern endpoint is calculated from the prescribed segment length and inferred strike. Other segments are connected sequentially, with one endpoint fixed to the adjacent segment and the other determined from segment length and strike.

formed in 1975–1984 (dashed rectangle 1 in Figures 5a and 5b). The other two (solid rectangles in Figure 5) are located near the geothermal areas of Bjarnarflag and Krafla (Figures 5c–5f). Vertical residuals within the Krafla caldera (Figure 5e) show discrepancies between InSAR and GNSS, reflecting their different lengths of observation periods, especially with an inflation period during 2018–2022 reported by Lanzi et al. (2023). Analysis of InSAR LOS displacement time series (Figure S15 in Supporting Information S1) further supports these observations.

5. Discussion

5.1. Data and Model Uncertainties

In this study, we decompose InSAR velocities assuming a negligible contribution of north-component displacement to LOS velocities. We estimate the velocity bias resulting from this assumption (Figure S16 in Supporting Information S1), which turns out to be negligible in the near-east component (<0.01 mm/yr) and is small (<0.9 mm/yr) in the near-up component. Both are much smaller than the assigned InSAR uncertainties (1.8 mm/yr) and therefore have limited impact on the inversion results and their interpretation. Alternative approaches to account for the north-component displacements include projecting LOS velocities along the spreading direction derived from previous models, estimating the north-component velocities from GNSS observations (Watson et al., 2022), or deriving it from the inversion. However, we do not expect these to improve the inversion results significantly because of the small bias.

The inferred horizontal and vertical GIA scaling factors are 5.83 and 0.60, respectively. The difference between these values likely reflects limitations of the GIA model rather than a physical difference between the two components. The Auriac (2014) model adopts a relatively simple three-layered Earth structure and constrains Earth properties using deformation data near the Vatnajökull glacier (Figure 1a). Given the complex crustal and mantle heterogeneity and the large distance (>100 km) between the Krafla area and the Vatnajökull glacier, the

Figure 4. Plate boundary model constrained from Global Navigation Satellite System (GNSS) horizontal and InSAR near-east velocity fields. (a) Zoomed-in view of the inferred plate boundary axis shown in Figure 3c. The color gradient from light to dark blue indicates plate boundary segments from south to north. (b, c) Marginal posterior probability density functions (PDF) of locking depths (b) and strikes (c) of plate boundary segments. The vertical extent of each panel corresponds to latitude range of the segments in panel (a). Vertical dashed lines indicate the medians of the PDFs. (d–f) Marginal posterior PDFs of the spreading parameters and horizontal glacial isostatic adjustment (GIA) scaling factor. Vertical dashed lines indicate the medians of the PDFs. (g) Profiles of observed and modeled horizontal velocities for all plate boundary segments. GNSS sites and InSAR pixels are grouped according to the segment to which they are assigned, forming one-dimensional velocity profiles. InSAR-GIA and GNSS-GIA denote the InSAR and GNSS velocities corrected for GIA displacements, respectively. PB indicates the plate boundary model predictions. Orange dots and triangles largely overlap with gray dots and triangles. Note the different *y*-axis scales for the east (left) and north (right) velocity components.

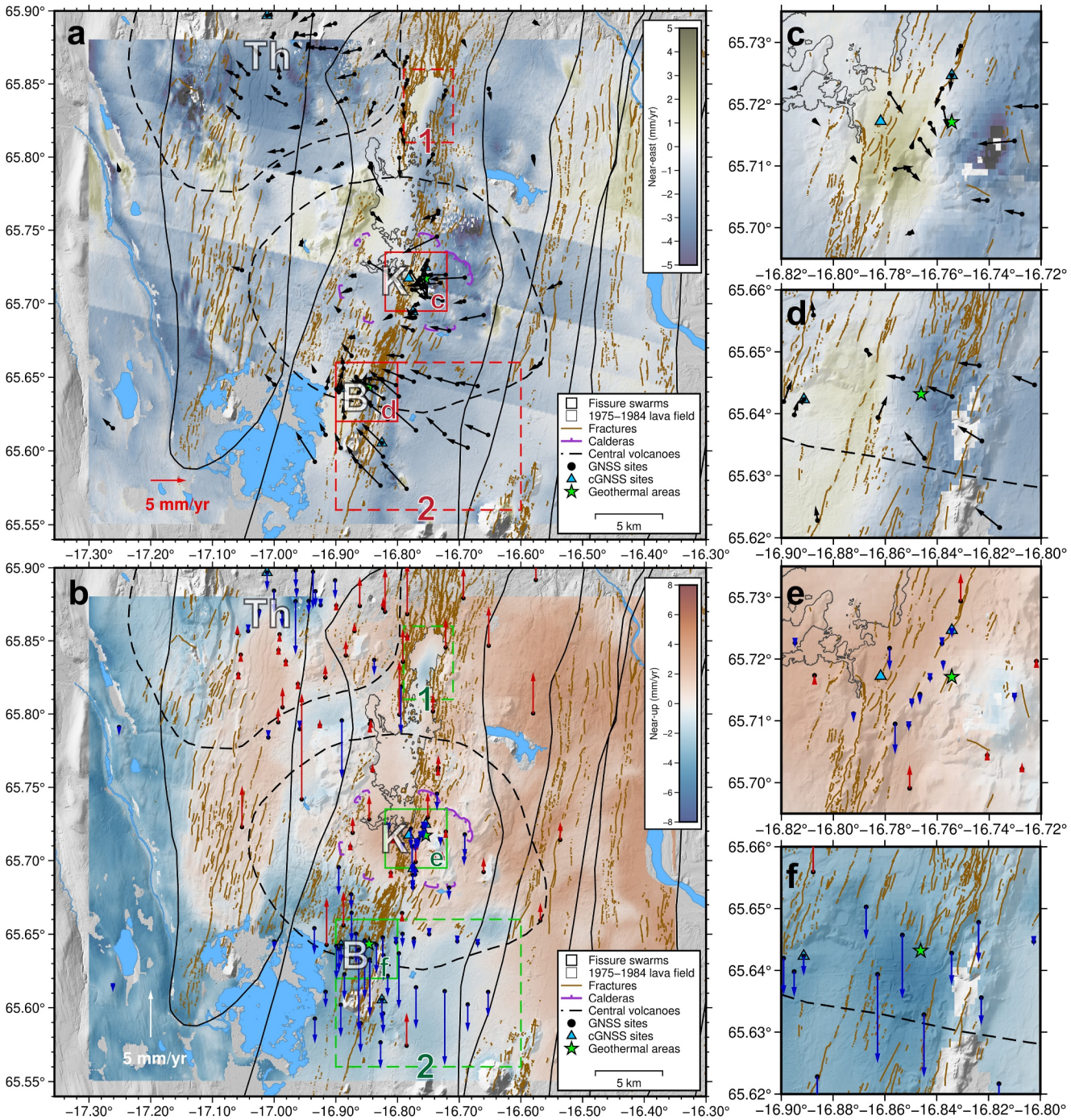

Figure 5. Horizontal (a) and vertical (b) residual velocity fields from Global Navigation Satellite System (arrows) and InSAR (colormaps). The residuals are the same as in Figures 3e and 3f. Gray lines centered symmetrically at the arrow tips in panel (b) indicate the uncertainties (95% confidence) of corresponding observation, same as in Figure 3b. Half of a gray line may be covered by the arrow body due to overlap. Rectangles indicate areas with local or regional residual patterns, where the solid rectangles correspond to panels (c–f). Th indicates the Þeistareykir (Theistareykir) volcanic system, K indicates the Krafla volcanic system and B indicates the Bjarnarflag geothermal field. (c, d) Zoomed-in view of the horizontal residual velocity fields at the geothermal areas. Symbols and colormaps have the same meaning as in panel (a). (e, f) Zoomed-in view of the vertical residual velocity fields at the geothermal areas. Symbols and colormaps have the same meaning as in panel (b).

model may not capture the local variability of GIA deformation in the study area. Previous studies have also suggested that GIA models may exhibit systematic difference between horizontal and vertical components, partly due to their sensitivities to Earth structure and simplifications in modeling approaches (e.g., Li et al., 2021; Spaans

21699356, 2026, 8, Downloaded from https://agupubs.onlinelibrary.wiley.com/doi/10.1029/2026JB034040 by Technical University Delft, Wiley Online Library on [02/09/2026]. See the Terms and Conditions (https://onlinelibrary.wiley.com/terms-and-conditions) on Wiley Online Library for rules of use; OA articles are governed by the applicable Creative Commons License

21699356, 2026, 8, Downloaded from https://agupubs.onlinelibrary.wiley.com/doi/10.1029/2026JB034040 by Technical University Delft, Wiley Online Library on [02/09/2026]. See the Terms and Conditions (https://onlinelibrary.wiley.com/terms-and-conditions) on Wiley Online Library for rules of use; OA articles are governed by the applicable Creative Commons License

et al., 2015). We therefore interpret the scaling factors as empirical adjustments that compensate for such model mismatches, which can behave differently for the horizontal and vertical components.

The model uncertainties in Table 1 result from the second-step inversion and therefore do not include uncertainty propagation from the first-step inversion. We assess the impact of geometric uncertainty in the plate-boundary axis in Text S1 in Supporting Information S1. These sensitivity tests suggest that variations in axis geometry introduce additional uncertainties of ∼0.5 km in locking depth, ∼1° in spreading direction, and up to ∼1 mm/yr in spreading rate, but do not alter the inferred first-order characteristics of plate divergence.

5.2. Model Assumptions and Their Implications

In our study, we first model the plate boundary deformation and then evaluate residual deformation patterns. This is different from the approach of Drouin, Sigmundsson, Ófeigsson, et al. (2017), where they corrected for known local deformation sources before inferring plate spreading. At Krafla, plate spreading is nearly perpendicular to the plate boundary axis, with obliquity angle α of ∼90° and deviations of <5° for all the segments. Thus, the east-component velocities primarily control the inversion of spreading parameters and locking depths. Although deep deformation sources, such as the 21.5 km deflation source modeled by Drouin, Sigmundsson, Ófeigsson, et al. (2017), could bias locking depth estimates, comparison between the observed east-component velocity profile and model predictions that include such a deep source (Figure S17a in Supporting Information S1). Additionally, synthetic data experiments suggest that deformation originating from shallow sources (≤2.5 km depth) affects the inferred locking depths by less than 15% (Figure S17b in Supporting Information S1).

The back slip model is a kinematic representation of plate boundary deformation and involves several simplifying assumptions. The model accounts for plate boundary deformation on a single vertical plane along the rift axis and therefore provides an approximation of deformation that does not include distributed or depth-dependent processes within the rift system (Lanzi et al., 2024). In nature, below the locking depth, ductile processes separate the plates over a finite width, whereas the model idealizes this by directly prescribing the relative displacement of the plates. In addition, we assume that deformation at each ground point is controlled by only one plate boundary segment, simplifying the mechanical coupling between adjacent segments. These simplifications enable regional-scale modeling but may reduce the model accuracy near the segment endpoints and limit the model's ability to reflect dynamic processes.

In our modeling approach, each plate boundary segment constrains the data points within its spatial extent along the spreading direction, while the northernmost and southernmost segments are assumed to continue beyond the model domain following their local strikes. Compared to a model that connects all segments and jointly evaluates deformation at all points using finite fault back slip from the Okada (1992) model, our approach generates velocity fields with similar large-scale patterns to the connected-segment model while producing sharper transitions near segment boundaries, rather than the smooth, gradual velocity fields from the connected-segment model (Figure S18 in Supporting Information S1). This approach preserves short-wavelength deformation signals associated with individual segments, allowing segment-scale variations in locking depth to be better resolved. The differences between the two approaches are small relative to the observed velocities, indicating that the independent-segment approximation is adequate for the inversion.

5.3. Inferred Plate Boundary Axis

The modeled plate boundary axis aligns with the areas with recent eruptive fissures mapped by Hjartardóttir et al. (2012) (Figure 4a). This alignment may reflect an interplay between tensile stress accumulation and crustal weakness at these fissures, as stress tends to localize there while magma intrusions further exploit these structures (e.g., Greiner et al., 2023, 2025). Compared to previous two-segment boundary models constrained solely by GNSS or InSAR data (green and red dashed lines in Figure 3c; Drouin & Sigmundsson, 2019; Drouin, Sigmundsson, Ófeigsson, et al., 2017), our inferred plate boundary axis better captures the local stress field. Namely, the strikes of inferred axis segments range from N7.8°W to N10.8°E, consistent with fracture orientations summarized by Corti et al. (2021), which have an average of N10.1°E and a standard deviation of 17.5°. Specifically, the increase in strike angles of axis segment S1 south of the Krafla central volcano to segments S2–S4 within the central volcano (Figure 4a) corresponds well with the observed trend of increasing fracture azimuths. The strikes of axis segments S5–S6 in Figure 4a change from NNE–SSW to NNW–SSE, consistent with greater abundance of NNW–SSE oriented fractures north of the Krafla central volcano than in the south (Corti

21699356, 2026, 8, Downloaded from https://agupubs.onlinelibrary.wiley.com/doi/10.1029/2026JB034040 by Technical University Delft, Wiley Online Library on [02/09/2026]. See the Terms and Conditions (https://onlinelibrary.wiley.com/terms-and-conditions) on Wiley Online Library for rules of use; OA articles are governed by the applicable Creative Commons License

et al., 2021; Hjartardóttir et al., 2012). This may reflect a local stress regime influenced by the intersection between the Krafla fissure swarm and the prolongation of the transform system further north of the study area.

Additionally, we evaluate a potential plate boundary geometry that includes a transverse structure within the Krafla caldera. Árnason (2020) proposed a possible WNW–ESE-striking transverse structure in the southern half of the Krafla caldera, based on anomalies in the electrical resistivity and a low-density structure in the gravity model. Seismic tomography also suggests a high P-wave to S-wave velocity ratio in this area (Schuler et al., 2015). Here we modify segment S3 to represent such a structure (Figure S19 in Supporting Information S1) and rerun the second-step inversion. The resulting model infers a spreading rate differing by <0.5 mm/yr and a spreading direction differing by <1° from the model presented in Section 4. However, because the strike of the transverse structure is nearly parallel to the spreading direction, its locking depth is poorly constrained. Moreover, this alternative model fits the deformation statistically worse with a smaller likelihood value than the model presented in Section 4 (larger likelihood value indicates better fit). Although the existence and role of this structure remains debated, our result suggests that it does not significantly influence the regional deformation pattern. Possible explanations include that the strike of the feature is too close to the plate spreading direction to be well constrained with our data sets, the feature is too small to be resolved in this study (∼1.5 km wide and <5 km long; Martinez-Garcia et al., 2025), or that it only affects the shallowest crust above the locking depth (Glück et al., 2025; Schuler et al., 2015).

5.4. Inferred Spreading Parameters

The inferred spreading direction falls within the range of 273°–292° predicted by global plate motion models but is smaller than the 288°–296° range derived from earlier regional models (Figure S20 in Supporting Information S1; Barreto et al., 2025; Drouin, Sigmundsson, Ófeigsson, et al., 2017; Metzger & Jónsson, 2014; Metzger et al., 2011). This discrepancy may be explained by the relatively large scaling factor (5.83) for GIA horizontal deformation in our model, compared to 3.2 in Drouin, Sigmundsson, Ófeigsson, et al. (2017). A higher scaling factor means that the inversion attributes a larger part of the observed northward motions to GIA, thereby reducing the inferred spreading azimuth (more E–W oriented). Note that some regional models did not account for GIA deformation because of the long distance from glaciers and uncertainties in GIA models, as they focused on a region further north (e.g., Barreto et al., 2025; Metzger & Jónsson, 2014), while Drouin, Sigmundsson, Ófeigsson, et al. (2017) applied a uniform scaling factor for GIA deformation over about 150 km distance. Our results highlight the need for a more accurate GIA model.

Our inferred spreading rate lies near the lower end of the 19–21 mm/yr range suggested by regional models (Barreto et al., 2025; Metzger & Jónsson, 2014; Metzger et al., 2011, 2013) but at the higher end of the average estimates from global models (Figure S20 in Supporting Information S1). Two causes may explain the larger spreading rate inferred across the Krafla volcanic system: (i) Decayed post-rifting viscoelastic relaxation of the 1975–1984 rifting episode may continue to contribute millimeter-level extension every year up to ∼60 km away from the rift (e.g., Ali et al., 2014; Hofton & Foulger, 1996; Li et al., 2022). The regionally elevated spreading rate may induce minor contraction further away from the rift. However, contraction with a rate difference of only 1–2 mm/yr, when distributed over a large area, is likely below the observational precision, may occur beyond the spatial extent of this study, or may be accommodated by existing shallow crustal structures such as normal faults (Ducrocq et al., 2024) or ductile processes at depth. (ii) GIA deformation, if not fully modeled, may influence the estimation of regional spreading parameters, especially near plate boundaries where the crust is weak and heterogeneous and the lithospheric thickness varies spatially (e.g., Klemann et al., 2008; Vardić et al., 2022; Yuan & Zhong, 2025). (iii) Because the observations are confined to the near- to mid-field of the plate boundary, the inferred spreading rate may incorporate regional variations in plate divergence rather than representing purely far-field rigid plate motion.

5.5. Inferred Locking Depth Variation

Figure 6 compares the spatial variations in the inferred locking depth with the seismicity during 2002–2022 and the surface widening during the 1975–1984 Krafla rifting episode. Two profiles are outlined based on the depth distribution of seismicity inferred by Guðnason et al. (2023), one indicating the depth range where most (∼90%) earthquakes occur, and the other approximating the maximum depth of seismicity (orange and brown lines in Figure 6, respectively). The inferred locking depth is referenced to the ground surface in above sections, while the

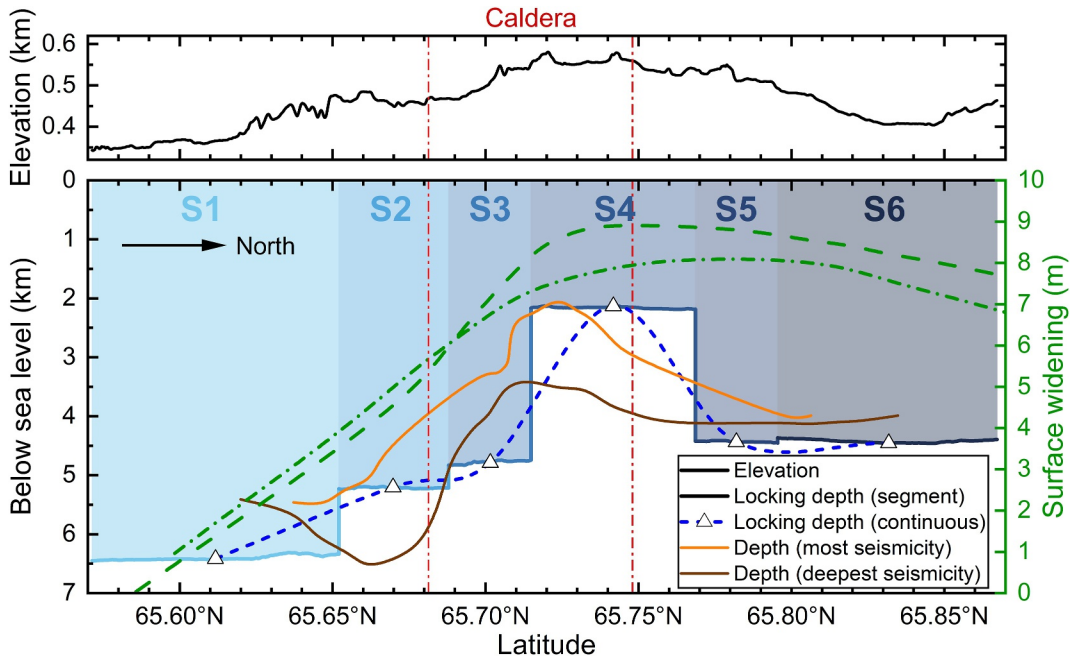

Figure 6. Comparison between the inferred plate boundary locking depth, the depth distribution of seismicity during 2006–2022 and the surface widening during the 1975–1984 rifting episode. The vertical dash-dotted red lines indicate the north and south rims of the Krafla caldera. The blue solid lines with varying intensity represent the inferred locking depth of different axis segments, where more southern segments correspond to lighter the blue color. Above the blue lines are boxes filled to the top with the same color, showing the depth range of the back slip dislocation. The triangles are the midpoints of the segments at their locking depths, fitted with a modified Bézier curve (blue dashed line; Kocić, 1991) to form an indicative continuous locking depth profile. Depth (most seismicity) indicates that most earthquakes occur shallower than this depth, while depth (deepest seismicity) outlines the deepest seismicity at Krafla. Dashed and dash-dotted green lines shows the surface widening during the 1975–1984 rifting episode estimated by Tryggvason (1984) and Hollingsworth et al. (2012), respectively, referring to the right vertical axis. The depth of seismicity is drawn based on Guðnason et al. (2023). The surface elevation is extracted along the plate boundary axis from the Digital Elevation Model by LMÍ (2020).

seismicity distribution in Guðnason et al. (2023) is referenced to the sea level. For better comparison, we add the surface elevation to the inferred the locking depth in Figure 6.

Both locking depth of plate boundary and depth distribution of seismicity reflect the brittle-ductile transition within the crust. The general trends of the blue, orange and brown lines in Figure 6 show mutual consistency, with shallowest depths beneath the Krafla caldera, and deepening laterally away from the caldera. The inferred shallowest locking depth of ∼2.1 km below sea level within and north of the Krafla caldera, together with most seismicity above ∼2 km depth, suggests shallow rheological changes. This is probably caused by elevated temperature and high pore-fluid pressure in the crust beneath the Krafla caldera, related to supercritical geothermal fluids and shallow magma bodies (e.g., Andajani et al., 2023; Eggertsson et al., 2020; Mortenson et al., 2010; Scott et al., 2015). High temperature enhances inelastic deformation, while high pore pressure reduces effective stress and favors distributed cataclastic flow over localized brittle faulting, shifting the brittle–ductile transition to shallower depths (e.g., Castagna et al., 2018; Parisio et al., 2019). Our result validates the deepened elastic-viscoelastic interface away from the Krafla caldera along the fissure swarm assumed in the regional subsidence model by Lanzi et al. (2024). The inferred shallowest locking depth is shifted northward compared to the seismicity, either reflecting the effect of recently intruded dike at shallow depth during the Krafla rifting episode (green curves in Figure 6) or affected by how the plate boundary is segmented.

Locking depth affects the style of stress accumulation and can influence how the plate divergence is accommodated at different locations along the plate boundary. Shallow locking depths produce steep gradients of horizontal deformation velocity, leading to concentrated strain accumulation and localized tensile stress, facilitating magma intrusions. Figure 6 illustrates that both the inferred shallowest locking depth and the maximum cumulative surface widening during the 1975–1984 rifting episode occurs within and north of the Krafla caldera.

21699356, 2026, 8, Downloaded from https://agupubs.onlinelibrary.wiley.com/doi/10.1029/2026JB034040 by Technical University Delft, Wiley Online Library on [02/09/2026]. See the Terms and Conditions (https://onlinelibrary.wiley.com/terms-and-conditions) on Wiley Online Library for rules of use; OA articles are governed by the applicable Creative Commons License

21699356, 2026, 8, Downloaded from https://agupubs.onlinelibrary.wiley.com/doi/10.1029/2026JB034040 by Technical University Delft, Wiley Online Library on [02/09/2026]. See the Terms and Conditions (https://onlinelibrary.wiley.com/terms-and-conditions) on Wiley Online Library for rules of use; OA articles are governed by the applicable Creative Commons License

Seismic observations and a model of repeated lateral dikes have indicated that dikes started lateral propagation in the northern part of the Krafla caldera during its 1975–1984 rifting episode (Einarsson & Brandsdóttir, 2021; Yang et al., 2025). Petrochemical evidence of bimodal eruptive products across the north caldera rim from the Krafla rifting episode further suggests magma mixing and supply from different depths (Rooyakkers et al., 2024). Magma intrusions into such a stress-localized area promote the development of a magma domain, consisting of partial melt, magma mush and hot solid rock (Sigmundsson et al., 2024). The inferred shallowest locking depth (∼3.5 km) within the caldera coincides with such a magma domain, inferred from geodetic, seismological, petrochemical and drilling observations (e.g., Einarsson, 1978; Heimisson et al., 2015; Kim et al., 2020; Mortenson et al., 2010; Rooyakkers et al., 2024; Schuler et al., 2015; Tryggvason, 1980). Stress localization further aids the maintenance of this domain by reducing confining pressure (Eichelberger & Carrigan, 2023). Conversely, dike intrusions and the presence of the magma domain weaken the crust and influence rheology around the caldera, reinforcing tensile stress accumulation. Together, these highlight the volcano-tectonic interactions in controlling ground deformation at volcanoes in a plate boundary zone.

5.6. Implications of Residual Deformation Patterns

Among the three local deflation signals in the residual velocity fields (Figure 5), two coincide with the geothermal areas of Bjarnarflag and Krafla (solid rectangles in Figures 5 and 5c–5f) and are likely associated with geothermal exploitation (e.g., Drouin, Sigmundsson, Verhagen, et al., 2017; Sturkell et al., 2008). The third signal, located at the northernmost part of the lava field formed during the 1975–1984 rifting episode (dashed rectangle 1 in Figure 5), may instead reflect post-emplacement processes such as thermal contraction (Sigmundsson et al., 1997), mechanical compaction (Ebmeier et al., 2012), or surface loading effects related to lava emplacement (e.g., Grapenthin et al., 2010).

Both observed and residual vertical velocities in Figures 3b and 3f show that uplift east of the Krafla fissure swarm is systematically larger than that to the west. This asymmetry may reflect heterogeneous GIA deformation across the plate boundary, potentially related to viscosity contrasts between the two plates (e.g., Vaghri & Hearn, 2012). Such rheological variations could lead to different viscoelastic responses to surface load changes. A GIA model that accounts for lithospheric heterogeneity would be required to further evaluate this interpretation.

Figure 5 indicates that the southeastern part of the study area exhibits relatively large residuals. GNSS horizontal residual vectors point northwestward with an average magnitude of ∼3 mm/yr, while vertical residuals from both InSAR and GNSS indicate subsidence of a few millimeters per year. The horizontal residual pattern is unlikely to be an artifact from the model configuration, because we implement infinitely long fault planes for the back slip dislocation (Figure 2b) to minimize deformation gradients near the endpoints of plate boundary segments. Three possible explanations may account for the regional residual deformation near Bjarnarflag: (i) plate spreading distributed across en-echelon, offset rift zones associated with the transition from the Krafla volcanic system to systems further south; however, this mechanism alone is unlikely to explain the observed subsidence; (ii) an unmodeled deflation source, potentially located deeper than the exploited geothermal system; and (iii) spatially distributed shallow deflation associated with the Bjarnarflag geothermal area, which may produce broad subsidence and associated horizontal contraction, as observed in the Reykjanes Peninsula, SW Iceland (e.g., Keiding et al., 2010; Parks et al., 2020).

Figures 4g and 5a suggest a north–south shortening of the Krafla fissure swarm centered on the central volcano. This pattern was previously explained using a deep deflation source by Drouin, Sigmundsson, Ófeigsson, et al. (2017). An alternative explanation for this north–south shortening is crustal heterogeneity along the fissure swarm, where variations in viscosity or rigidity generate strike-parallel localized contraction toward the central volcano. Such a systematic pattern produces opposite effects north and south of the source, which tend to cancel out in the second-step inversion and therefore should not considerably affect the inferred spreading parameters.

6. Conclusion

We evaluate plate divergence and volcano-tectonic interaction along the Krafla volcanic system by constraining a six-segment plate boundary model using long-term deformation velocity fields from GNSS data (2002–2024) and Sentinel-1 SAR interferograms (2015–2023). The model is established through a kinematic back slip model and a two-step Bayesian inversion strategy. The model considers GIA deformation and jointly solves for the axis geometry, spreading parameters and segmental locking depths. The inferred plate boundary axis strikes N1.2° to

N10.8°E within and south of the Krafla central volcano, and changes to N4.9$^{+2.7}_{-1.0}$°W north of it, aligning with the orientations of mapped fractures. Based on the preferred axis geometry, we estimate a spreading rate of 19.2$^{+0.2}_{-0.2}$ mm/yr in an azimuth of 283.5$^{+0.2}_{-0.2}$° (formal uncertainties corresponding to the 95% confidence interval from the Bayesian inversion). We infer locking depths to be shallowest beneath and north of the Krafla caldera at ∼2.7 km below surface, increasing to ∼4.9 and ∼6.8 km north and south of the central volcano, respectively. Such variation is consistent with the depth distribution of seismicity, indicating an up-doming crustal structure along the Krafla fissure swarm. The shallowest locking depth coincides with the maximum surface widening during the 1975–1984 rifting episode and the area where dikes started lateral propagation, implying that tensile stress accumulation along the plate boundary facilitates dike intrusions. Residual velocity fields reveal three local deflation patterns, two related to geothermal activities at Krafla and Bjarnarflag geothermal fields and another related to 1975–1984 lava field.

Conflict of Interest

The authors declare no conflicts of interest relevant to this study.

Acknowledgments

We thank Editor Shin-Chan Han for handling the manuscript, Associate Editor Kristel Chanard for helpful suggestions, and Jeffrey T. Freymueller and an anonymous reviewer for their important comments. This study received funding from the European Union's Horizon 2020 research and innovation programme under grant agreement No. 858092 (IMPROVE project). J.S.-A. thanks the National Agency for Research and Development (ANID) for the support with the Scholarship program, Beca de Doctorado en el Extranjero 72210412. J.G.'s contributions have been supported by Y. Lavallee's European Research Council (ERC) Consolidator Grant MODERATE under grant agreement No. 101001065. We acknowledge Landsvirkjun for collaboration and partial financial support on this research and the GNSS observations. We thank Sveinbjörn Steinþórsson for excellent field support for the GNSS measurements, and collaboration on the Krafla GNSS surveys in 2012–2024 with Delft University of Technology, through their summer course program, led by Paco Lopez Dekker, Freek van Leijen, and others. COMET is the UK Natural Environment Research Council's (NERC) Centre for the Observation and Modelling of Earthquakes, Volcanoes and Tectonics, a partnership between UK Universities and the British Geological Survey (https://comet.nerc.ac.uk). We acknowledge Milan Lazecky (University of Leeds), Tianyuan Zhu and Simon Orrego Astudillo (University of Bristol) for supports on InSAR data processing. We thank Corné Kreemer and Raphaël Grandin for suggestions to improve the manuscript. We thank Andrew Hooper, Alejandra Barreto, Þorbjörg Ágústsdóttir, Egill Árni Guðnasson, Elisabeth Glück, and Patricia Fehrentz for discussions. The global plate motions are calculated with GAGE Plate Motion Calculator (https://www.unavco.org/software/geodetic-utilities/plate-motion-calculator/plate-motion-calculator.html). Maps are plotted with the Generic Mapping Tools (Wessel et al., 2019).

Availability Statement

GAMIT/GLOBK software for GNSS data processing is available upon request under license from https://geoweb.mit.edu/gg/license.php. LiCSBAS software for InSAR time-series analysis is available at https://github.com/yumorishita/LiCSBAS. Sentinel-1 interferograms processed by COMET are available through https://comet.nerc.ac.uk/comet-lics-portal/. The original version of the GBIS software is available at https://comet.nerc.ac.uk/geodetic-bayesian-inversion-software-gbis/. The Hector software (Bos et al., 2013) for GNSS time series analysis and noise assessment is available at https://teromovigo.com/product/hector/.The long-term velocity fields at Krafla derived from GNSS (2002–2024) and InSAR (2015–2023) are available at the Zenodo (Yang et al., 2026).

References

Albino, F., Biggs, J., Yu, C., & Li, Z. (2020). Automated methods for detecting volcanic deformation using Sentinel-1 InSAR time series illustrated by the 2017–2018 unrest at Agung, Indonesia. *Journal of Geophysical Research: Solid Earth*, *125*(2), e2019JB017908. https://doi.org/10.1029/2019JB017908

Albino, F., Gremion, S., Pinel, V., Bouygues, P., Peltier, A., Beauducel, F., et al. (2025). Benefits of GNSS local observations compared to global weather-based models for InSAR tropospheric corrections over tropical volcanoes: Case studies of Piton de la Fournaise and Merapi. *Journal of Geophysical Research: Solid Earth*, *130*(4), e2024JB028898. https://doi.org/10.1029/2024JB028898

Ali, S. T., Feigl, K. L., Carr, B. B., Masterlark, T., & Sigmundsson, F. (2014). Geodetic measurements and numerical models of rifting in Northern Iceland for 1993–2008. *Geophysical Journal International*, *196*(3), 1267–1280. https://doi.org/10.1093/gji/ggt462

Altamimi, Z., Métivier, L., Rebischung, P., Rouby, H., & Collilieux, X. (2017). ITRF2014 plate motion model. *Geophysical Journal International*, *209*(3), 1906–1912. https://doi.org/10.1093/gji/ggx136

Altamimi, Z., Rebischung, P., Métivier, L., & Collilieux, X. (2016). ITRF2014: A new release of the International Terrestrial Reference Frame modeling nonlinear station motions. *Journal of Geophysical Research: Solid Earth*, *121*(8), 6109–6131. https://doi.org/10.1002/2016JB013098

Andajani, R. D., Tsuji, T., Ikeda, T., Matsumoto, S., Kitamura, K., & Nishijima, J. (2023). Tracking supercritical geothermal fluid distribution from continuous seismic monitoring. *Scientific Reports*, *13*(1), 8370. https://doi.org/10.1038/s41598-023-35159-8

Argus, D. F., Gordon, R. G., Heflin, M. B., Ma, C., Eanes, R. J., Willis, P., et al. (2010). The angular velocities of the plates and the velocity of the Earth's centre from space geodesy. *Geophysical Journal International*, *180*(3), 913–960. https://doi.org/10.1111/j.1365-246X.2009.04463.x

Árnadóttir, T., Lund, B., Jiang, W., Geirsson, H., Björnsson, H., Einarsson, P., & Sigurdsson, T. (2009). Glacial rebound and plate spreading: Results from the first countrywide GPS observations in Iceland. *Geophysical Journal International*, *177*(2), 691–716. https://doi.org/10.1111/j.1365-246X.2008.04059.x

Árnason, K. (2020). New conceptual model for the magma-hydrothermal-tectonic system of Krafla, NE Iceland. *Geosciences*, *10*(1), 34. https://doi.org/10.3390/geosciences10010034

Augustin, N., van der Zwan, F. M., Devey, C. W., & Brandsdóttir, B. (2021). 13 million years of seafloor spreading throughout the Red Sea Basin. *Nature Communications*, *12*(1), 2427. https://doi.org/10.1038/s41467-021-22586-2

Auriac, A. (2014). *Solid Earth response to ice retreat and glacial surges in Iceland inferred from satellite radar interferometry and finite element modelling* (PhD thesis). University of Iceland.

Bagnardi, M., & Hooper, A. (2018). Inversion of surface deformation data for rapid estimates of source parameters and uncertainties: A Bayesian approach. *Geochemistry, Geophysics, Geosystems*, *19*(7), 2194–2211. https://doi.org/10.1029/2018GC007585

Barreto, A., Viltres, R., Matrau, R., Metzger, S., Ófeigsson, B. G., Liu, S., et al. (2025). Interseismic deformation of the Húsavík–Flatey fault (North Iceland) from two decades of GNSS data. *Geophysical Journal International*, *241*(3), 1663–1679. https://doi.org/10.1093/gji/ggaf106

Bennett, E. N., Jenner, F. E., Millet, M.-A., Cashman, K. V., & Lissenberg, C. J. (2019). Deep roots for mid-ocean-ridge volcanoes revealed by plagioclase-hosted melt inclusions. *Nature*, *572*(7768), 235–239. https://doi.org/10.1038/s41586-019-1448-0

Björnsson, A., Saemundsson, K., Einarsson, P., Tryggvason, E., & Grönvold, K. (1977). Current rifting episode in north Iceland. *Nature*, *266*(5597), 318–323. https://doi.org/10.1038/266318a0

Blewitt, G., & Lavallée, D. A. (2002). Effect of annual signals on geodetic velocity. *Journal of Geophysical Research*, *107*(B7), ETG9-1–ETG9-11. https://doi.org/10.1029/2001JB000570

21699356, 2026, 8, Downloaded from https://agupubs.onlinelibrary.wiley.com/doi/10.1029/2026JB034040 by Technical University Delft, Wiley Online Library on [02/09/2026]. See the Terms and Conditions (https://onlinelibrary.wiley.com/terms-and-conditions) on Wiley Online Library for rules of use; OA articles are governed by the applicable Creative Commons License

Boehm, J., Werl, B., & Schuh, H. (2006). Troposphere mapping functions for GPS and very long baseline interferometry from European Centre for Medium-Range Weather Forecasts operational analysis data. *Journal of Geophysical Research*, *111*(B2), B02406. https://doi.org/10.1029/2005JB003629

Bos, M. S., Fernandes, R. M. S., Williams, S. D. P., & Bastos, L. (2013). Fast error analysis of continuous GNSS observations with missing data. *Journal of Geodesy*, *87*(4), 351–360. https://doi.org/10.1007/s00190-012-0605-0

Cao, Y., Jónsson, S., & Hreinsdóttir, S. (2023). Iceland kinematics from InSAR. *Journal of Geophysical Research: Solid Earth*, *128*(3), e2022JB025546. https://doi.org/10.1029/2022JB025546

Castagna, A., Ougier-Simonin, A., Benson, P. M., Browning, J., Walker, R. J., Fazio, M., & Vinciguerra, S. (2018). Thermal damage and pore pressure effects of the brittle–ductile transition in Comiso limestone. *Journal of Geophysical Research: Solid Earth*, *123*(9), 7644–7660. https://doi.org/10.1029/2017JB015105

COMSOL. (2022). *COMSOL multiphysics® v6.1*. COMSOL AB. Retrieved from https://www.comsol.com

Corti, N., Bonali, F. L., Pasquaré Mariotto, F., Tibaldi, A., Russo, E., Hjartardóttir, Á. R., et al. (2021). Fracture kinematics and Holocene stress field at the Krafla Rift, northern Iceland. *Geosciences*, *11*(2), 101. https://doi.org/10.3390/geosciences11020101

DeMets, C., Gordon, R. G., & Argus, D. F. (2010). Geologically current plate motions. *Geophysical Journal International*, *181*(1), 1–80. https://doi.org/10.1111/j.1365-246X.2009.04491.x

DeMets, C., Gordon, R. G., Argus, D. F., & Stein, S. (1994). Effect of recent revisions to the geomagnetic reversal time scale on estimates of current plate motions. *Geophysical Research Letters*, *21*(20), 2191–2194. https://doi.org/10.1029/94GL02118

Denis, D., McCarthy, D. D., & Petit, G. (2004). *IERS conventions (2003)* (IERS Technical Note 32). IERS Convention Center.

Doin, M.-P., Lodge, F., Guillaso, S., Jolivet, R., Lasserre, C., Ducret, G., et al. (2011). Presentation of the small baseline NSBAS processing chain on a case example: The Etna deformation monitoring from 2003 to 2010 using Envisat data. In *Proceedings of the FRINGE 2011 workshop, Frascati, Italy, 19–23 September* (ESA SP-697). European Space Agency (ESA).

Dragoni, M., & Magnanensi, C. (1989). Displacement and stress produced by a pressurized, spherical magma chamber surrounded by a visco-elastic shell. *Physics of the Earth and Planetary Interiors*, *56*(3–4), 316–328. https://doi.org/10.1016/0031-9201(89)90166-0

Drouin, V., & Sigmundsson, F. (2019). Countrywide observations of plate spreading and glacial isostatic adjustment in Iceland inferred by Sentinel-1 radar interferometry, 2015–2018. *Geophysical Research Letters*, *46*(14), 8046–8055. https://doi.org/10.1029/2019GL082629

Drouin, V., Sigmundsson, F., Ófeigsson, B. G., Hreinsdóttir, S., Sturkell, E., & Einarsson, P. (2017). Deformation in the Northern Volcanic Zone of Iceland 2008–2014: An interplay of tectonic, magmatic, and glacial isostatic deformation. *Journal of Geophysical Research: Solid Earth*, *122*(4), 3158–3178. https://doi.org/10.1002/2016JB013206

Drouin, V., Sigmundsson, F., Verhagen, S., Ófeigsson, B. G., Spaans, K., & Hreinsdóttir, S. (2017). Deformation at Krafla and Bjarnarflag geothermal areas, Northern Volcanic Zone of Iceland, 1993–2015. *Journal of Volcanology and Geothermal Research*, *344*, 92–105. https://doi.org/10.1016/j.jvolgeores.2017.06.013

Ducrocq, C., Árnadóttir, Þ., Einarsson, P., Jónsson, S., Drouin, V., Geirsson, H., & Hjartardóttir, Á. R. (2024). Widespread fracture movements during a volcano-tectonic unrest: The Reykjanes Peninsula, Iceland, from 2019–2021 TerraSAR-X interferometry. *Bulletin of Volcanology*, *86*(2), 14. https://doi.org/10.1007/s00445-023-01699-0

Ebmeier, S. K., Biggs, J., Mather, T. A., Elliott, J. R., Wadge, G., & Amelung, F. (2012). Measuring large topographic change with InSAR: Lava thicknesses, extrusion rate and subsidence rate at Santiaguito volcano, Guatemala. *Earth and Planetary Science Letters*, *335–336*, 216–225. https://doi.org/10.1016/j.epsl.2012.04.027

Eggertsson, G. H., Lavallée, Y., Kendrick, J. E., & Markússon, S. H. (2020). Improving fluid flow in geothermal reservoirs by thermal and mechanical stimulation: The case of Krafla volcano, Iceland. *Journal of Volcanology and Geothermal Research*, *391*, 106351. https://doi.org/10.1016/j.jvolgeores.2018.04.008

Eichelberger, J. C., & Carrigan, C. R. (2023). What is the confining pressure of magma and what does this mean about depth and eruption? *AGU Fall Meeting Abstracts*, *2023*(195), V23D-0195. https://agu.confex.com/agu/fm23/meetingapp.cgi/Paper/1271150

Einarsson, P. (1978). S-wave shadows in the Krafla Caldera in NE-Iceland, evidence for a magma chamber in the crust. *Bulletin of Volcanology*, *41*(3), 187–195. https://doi.org/10.1007/BF02597222

Einarsson, P. (1991). Umbrotin við Kröflu 1975–89 (in Icelandic). In A. Garðarsson & Á. Einarsson (Eds.), *Náttúra Mývatns* (pp. 97–139). Hið íslenska náttúrufræðifélag.

Einarsson, P., & Brandsdóttir, B. (2021). Seismicity of the Northern Volcanic Zone of Iceland. *Frontiers in Earth Science*, *9*, 628967. https://doi.org/10.3389/feart.2021.628967

Elliott, J., Fang, J., Lazecky, M., Maghsoudi, Y., Ou, Q., Payne, J., et al. (2025). Deformation, strains and velocities for the Alpine–Himalayan Belt from trans-continental Sentinel-1 InSAR and GNSS. *EarthArXiv*. https://doi.org/10.31223/X5GX6B

European Space Agency (ESA). (2020). Copernicus Digital Elevation Model (DEM) – 2020 release [Dataset]. *European Space Agency*. https://doi.org/10.5270/ESA-c5d3d65

Glück, E., Garambois, S., Vandemeulebrouck, J., Muzellec, T., Virieux, J., Mortensen, A. K., et al. (2025). Seismicity patterns and multi-scale imaging of Krafla, N–E Iceland, with local earthquake tomography. *Journal of Geophysical Research: Solid Earth*, *130*(5), e2024JB030425. https://doi.org/10.1029/2024JB030425

Grapenthin, R., Ófeigsson, B. G., Sigmundsson, F., Sturkell, E., & Hooper, A. (2010). Pressure sources versus surface loads: Analyzing volcano deformation signal composition with an application to Hekla volcano, Iceland. *Geophysical Research Letters*, *37*(20), L20310. https://doi.org/10.1029/2010GL044590

Greiner, S. H. M., Burchardt, S., Sigmundsson, F., Óskarsson, B. V., Galland, O., Geirsson, H., & Rhodes, E. (2023). Interaction between propagating basaltic dikes and pre-existing fractures: A case study in hyaloclastite from Dyrfjöll, Iceland. *Journal of Volcanology and Geothermal Research*, *442*, 107891. https://doi.org/10.1016/j.jvolgeores.2023.107891

Greiner, S. H. M., Galland, O., Sigmundsson, F., Burchardt, S., Geirsson, H., Pedersen, R., & Wen, X. (2025). The influence of variable host rock cohesion and magma viscosity on intrusion-fault interaction: Insights from laboratory models. *Journal of Geophysical Research: Solid Earth*, *130*(4), e2024JB029870. https://doi.org/10.1029/2024JB029870

Gudnason, E. Á., Drouin, V., Yang, Y., Sigmundsson, F., Ágústsdóttir, T., & Mortensen, A. K. (2024). Changes in seismicity and observed deformation related to inflation at the Theistareykir high-temperature geothermal field, NE Iceland, in 2023–2024. In *EGU General Assembly 2024, Vienna, Austria, 14–19 April 2024* (EGU24-19913). https://doi.org/10.5194/egusphere-egu24-19913

Guðnason, E. Á., Ágústsdóttir, Þ., Magnússon, R. L., & Gunnarsson, K. (2023). *Seismic monitoring in Krafla, Þeistareykir and Námafjall: October 2022 to November 2023 (LV-2023-060)*. Landsvirkjun. Retrieved from http://hdl.handle.net/10802/34603

Head, M., Hickey, J., Gottsmann, J., & Fournier, N. (2021). Exploring the impact of thermally controlled crustal viscosity on volcanic ground deformation. *Journal of Geophysical Research: Solid Earth*, *126*(8), 1–22. https://doi.org/10.1029/2020JB020724

21699356, 2026, 8, Downloaded from https://agupubs.onlinelibrary.wiley.com/doi/10.1029/2026JB034040 by Technical University Delft, Wiley Online Library on [02/09/2026]. See the Terms and Conditions (https://onlinelibrary.wiley.com/terms-and-conditions) on Wiley Online Library for rules of use; OA articles are governed by the applicable Creative Commons License

Heimisson, E. R., Einarsson, P., Sigmundsson, F., & Brandsdóttir, B. (2015). Kilometer-scale Kaiser effect identified in Krafla volcano, Iceland. *Geophysical Research Letters*, *42*(19), 7958–7965. https://doi.org/10.1002/2015GL065680

Herring, T. A., King, R. W., Floyd, M. A., & McClusky, S. C. (2018). *Introduction to GAMIT/GLOBK*. Massachusetts Institute of Technology. Retrieved from http://geoweb.mit.edu/gg/Intro_GG.pdf

Hjartardóttir, Á. R., Einarsson, P., Bramham, E., & Wright, T. (2012). The Krafla fissure swarm, Iceland, and its formation by rifting events. *Bulletin of Volcanology*, *74*(9), 2139–2153. https://doi.org/10.1007/s00445-012-0659-0

Hjartardóttir, Á. R., Einarsson, P., Magnúsdóttir, S., Björnsdóttir, Þ., & Brandsdóttir, B. (2015). Fracture systems of the Northern Volcanic Rift Zone, Iceland: An onshore part of the Mid-Atlantic plate boundary. In T. Wright, A. Ayele, D. J. Ferguson, T. Kidane, & C. Vye-Brown (Eds.), *Magmatic rifting and active volcanism* (Vol. 420(1), pp. 297–314). Geological Society of London. https://doi.org/10.1144/SP420.1

Hofton, M. A., & Foulger, G. R. (1996). Postrifting anelastic deformation around the spreading plate boundary, north Iceland: 1. Modeling of the 1987–1992 deformation field using a viscoelastic Earth structure. *Journal of Geophysical Research*, *101*(B11), 25403–25421. https://doi.org/10.1029/96JB02466

Hollingsworth, J., Leprince, S., Ayoub, F., & Avouac, J.-P. (2012). Deformation during the 1975–1984 Krafla rifting crisis, NE Iceland, measured from historical optical imagery. *Journal of Geophysical Research*, *117*(B11), B11407. https://doi.org/10.1029/2012JB009140

Jeffreys, H. (1939). *Theory of probability*. Clarendon Press.

Jóhannesson, H., & Sæmundsson, K. (2009). *Jarðfræðikort af Íslandi 1:600,000, höggun: Geological map of Iceland 1:600,000 – Tectonics*. Icelandic Institute of Natural History.

Keiding, M., Árnadóttir, T., Jónsson, S., Decriem, J., & Hooper, A. (2010). Plate boundary deformation and man-made subsidence around geothermal fields on the Reykjanes Peninsula, Iceland. *Journal of Volcanology and Geothermal Research*, *194*(4), 139–149. https://doi.org/10.1016/j.jvolgeores.2010.04.011

Kim, D., Brown, L. D., Árnason, K., Gudmundsson, Ó., Ágústsson, K., & Flóvenz, Ó. G. (2020). Magma "bright spots" mapped beneath Krafla, Iceland, using RVSP imaging of reflected waves from microearthquakes. *Journal of Volcanology and Geothermal Research*, *391*, 106365. https://doi.org/10.1016/j.jvolgeores.2018.04.022

Klemann, V., Martinec, Z., & Ivins, E. R. (2008). Glacial isostasy and plate motion. *Journal of Geodynamics*, *46*(3–5), 95–103. https://doi.org/10.1016/j.jog.2008.04.005

Kocić, L. M. (1991). Modification of Bézier curves and surfaces by degree-elevation technique. *Computer-Aided Design*, *23*(10), 692–699. https://doi.org/10.1016/0010-4485(91)90022-O

Landmælingar Íslands (LMÍ). (2020). *ÍslandsDEM, version 1.0, Landmælingar Íslands*. National Land Survey of Iceland. Retrieved from https://gatt.natt.is/geonetwork/srv/api/records/e6712430-a63c-4ae5-9158-c89d16da6361

Lanzi, C., Drouin, V., Sigmundsson, F., Geirsson, H., Hersir, G. P., Ágústsson, K., et al. (2023). Pressure increase at the magma-hydrothermal interface at Krafla caldera, North-Iceland, 2018–2020: Magmatic processes or hydrothermal changes? *Journal of Volcanology and Geothermal Research*, *440*, 107849. https://doi.org/10.1016/j.jvolgeores.2023.107849

Lanzi, C., Sigmundsson, F., Parks, M. M., Geirsson, H., & Drouin, V. (2024). Strain localization at volcanoes undergoing extension: Investigation of long-term deformation at Krafla and Askja volcanic systems in North Iceland. *Geophysical Research Letters*, *51*(21), e2024GL110299. https://doi.org/10.1029/2024GL110299

Lazecký, M., Spaans, K., González, P. J., Maghsoudi, Y., Morishita, Y., Albino, F., et al. (2020). LiCSAR: An automatic InSAR tool for measuring and monitoring tectonic and volcanic activity. *Remote Sensing*, *12*(15), 2430. https://doi.org/10.3390/rs12152430

Leonard, L. J., Hyndman, R. D., Mazzotti, S., Nykolaishen, L., Schmidt, M., & Hippchen, S. (2007). Current deformation in the northern Canadian Cordillera inferred from GPS measurements. *Journal of Geophysical Research*, *112*(B11), B11401. https://doi.org/10.1029/2007JB005061

Li, S., Grapenthin, R., Sigmundsson, F., Drouin, V., Hreinsdóttir, S., & Ófeigsson, B. G. (2022). Post-rifting relaxation during 2015–2020 following the Bárðarbunga-Holuhraun dike intrusion and eruption in Iceland. *Geophysical Research Letters*, *49*(13), e2022GL098977. https://doi.org/10.1029/2022GL098977

Li, S., Sigmundsson, F., Drouin, V., Parks, M. M., Ofeigsson, B. G., Jónsdóttir, K., et al. (2021). Ground deformation after a caldera collapse: Contributions of magma inflow and viscoelastic response to the 2015–2018 deformation field around Bárðarbunga, Iceland. *Journal of Geophysical Research: Solid Earth*, *126*(3), e2020JB020157. https://doi.org/10.1029/2020JB020157

López-Quiroz, P., Doin, M.-P., Tupin, F., Briole, P., & Nicolas, J.-M. (2009). Time series analysis of Mexico City subsidence constrained by radar interferometry. *Journal of Applied Geophysics*, *69*(1), 1–15. https://doi.org/10.1016/j.jappgeo.2009.02.006

Lyard, F., Lefevre, F., Letellier, T., & Francis, O. (2006). Modelling the global ocean tides: Modern insights from FES2004. *Ocean Dynamics*, *56*(5–6), 394–415. https://doi.org/10.1007/s10236-006-0086-x

Martinez-Garcia, A., Gottsmann, J., Wookey, J., Rust, A., Gudmundsson, M. T., & Lavallée, Y. (2025). 3D model of the shallow crustal density distribution of the Krafla volcanic system in Iceland. *Journal of Geophysical Research: Solid Earth*, *130*(7), e2025JB031670. https://doi.org/10.1029/2025JB031670

Metzger, S., & Jónsson, S. (2014). Plate boundary deformation in North Iceland during 1992–2009 revealed by InSAR time-series analysis and GPS. *Tectonophysics*, *634*, 127–138. https://doi.org/10.1016/j.tecto.2014.07.027

Metzger, S., Jónsson, S., Danielsen, G., Hreinsdóttir, S., Jouanne, F., Giardini, D., & Villemin, T. (2013). Present kinematics of the Tjörnes Fracture Zone, North Iceland, from campaign and continuous GPS measurements. *Geophysical Journal International*, *192*(2), 441–455. https://doi.org/10.1093/gji/ggs032

Metzger, S., Jónsson, S., & Geirsson, H. (2011). Locking depth and slip-rate of the Húsavík Flatey fault, North Iceland, derived from continuous GPS data 2006–2010. *Geophysical Journal International*, *187*(2), 564–576. https://doi.org/10.1111/j.1365-246X.2011.05176.x

Morishita, Y., Lazecky, M., Wright, T. J., Weiss, J. R., Elliott, J. R., & Hooper, A. (2020). LiCSBAS: An open-source InSAR time series analysis package integrated with the LiCSAR automated Sentinel-1 InSAR processor. *Remote Sensing*, *12*(3), 424. https://doi.org/10.3390/rs12030424

Mortensen, A., Grönvold, K., Gudmundsson, Á., Steingrímsson, B., & Egilson, T. (2010). Quenched silicic glass from well KJ-39 in Krafla, North-Eastern Iceland. In *Proceedings of the World Geothermal Congress* (pp. 1–6). International Geothermal Association.

Motagh, M., Shamshiri, R., Haghshenas Haghighi, M., Wetzel, H.-U., Akbari, B., Nahavandchi, H., et al. (2017). Quantifying groundwater exploitation induced subsidence in the Rafsanjan plain, southeastern Iran, using InSAR time-series and in situ measurements. *Engineering Geology*, *218*, 134–151. https://doi.org/10.1016/j.enggeo.2017.01.011

Nikolaidis, R. (2002). *Observation of geodetic and seismic deformation with the Global Positioning System* (PhD thesis). University of California, San Diego.

Okada, Y. (1985). Surface deformation due to shear and tensile faults in a half-space. *Bulletin of the Seismological Society of America*, *75*(4), 1135–1154. https://doi.org/10.1785/BSSA0750041135

Okada, Y. (1992). Internal deformation due to shear and tensile faults in a half-space. *Bulletin of the Seismological Society of America*, *82*(2), 1018–1040. https://doi.org/10.1785/BSSA0820021018

21699356, 2026, 8, Downloaded from https://agupubs.onlinelibrary.wiley.com/doi/10.1029/2026JB034040 by Technical University Delft, Wiley Online Library on [02/09/2026]. See the Terms and Conditions (https://onlinelibrary.wiley.com/terms-and-conditions) on Wiley Online Library for rules of use; OA articles are governed by the applicable Creative Commons License

Opheim, J. A., & Gudmundsson, A. (1989). Formation and geometry of fractures, and related volcanism, of the Krafla fissure swarm, northeast Iceland. *Geological Society of America Bulletin*, *101*(12), 1608–1622. https://doi.org/10.1130/0016-7606(1989)101<1608:FAGOFA>2.3.CO;2

Pagli, C., Wang, H., Wright, T. J., Calais, E., & Lewi, E. (2014). Current plate boundary deformation of the Afar rift from a 3-D velocity field inversion of InSAR and GPS. *Journal of Geophysical Research: Solid Earth*, *119*(11), 8562–8575. https://doi.org/10.1002/2014JB011391

Parisio, F., Vinciguerra, S., Kolditz, O., & Nagel, T. (2019). The brittle–ductile transition in active volcanoes. *Scientific Reports*, *9*(1), 143. https://doi.org/10.1038/s41598-018-36505-x

Parks, M. M., Sigmundsson, F., Sigurðsson, Ó., Hooper, A., Hreinsdóttir, S., Ófeigsson, B., & Michalczewska, K. (2020). Deformation due to geothermal exploitation at Reykjanes, Iceland. *Journal of Volcanology and Geothermal Research*, *391*, 106438. https://doi.org/10.1016/j.jvolgeores.2018.08.016

Rooyakkers, S. M., Carroll, K. J., Gutai, A. F., Winpenny, B., Bali, E., Guðfinnsson, G. H., et al. (2024). Hydraulically linked reservoirs simultaneously fed the 1975–1984 Krafla Fires eruptions: Insights from petrochemistry. *Earth and Planetary Science Letters*, *646*, 118960. https://doi.org/10.1016/j.epsl.2024.118960

Sæmundsson, K. (1991). Jarðfræði Kröflukerfisins (in Icelandic). In A. Garðarsson & A. Einarsson (Eds.), *Náttúra Mývatns* (pp. 24–95). Icelandic Nature Science Society.

Savage, J. C. (1983). A dislocation model of strain accumulation and release at a subduction zone. *Journal of Geophysical Research*, *88*(B6), 4984–4996. https://doi.org/10.1029/JB088iB06p04984

Schuler, J., Greenfield, T., White, R. S., Roecker, S. W., Brandsdóttir, B., Stock, J. M., et al. (2015). Seismic imaging of the shallow crust beneath the Krafla central volcano, NE Iceland. *Journal of Geophysical Research: Solid Earth*, *120*(10), 7156–7173. https://doi.org/10.1002/2015JB012350

Scott, S., Driesner, T., & Weis, P. (2015). Geologic controls on supercritical geothermal resources above magmatic intrusions. *Nature Communications*, *6*(1), 7837. https://doi.org/10.1038/ncomms8837

Sigmundsson, F., Einarsson, P., Hjartardóttir, Á. R., Drouin, V., Jónsdóttir, K., Árnadóttir, Þ., et al. (2020). Geodynamics of Iceland and the signatures of plate spreading. *Journal of Volcanology and Geothermal Research*, *391*, 106436. https://doi.org/10.1016/j.jvolgeores.2018.08.014

Sigmundsson, F., Parks, M., Geirsson, H., Hooper, A., Drouin, V., Vogfjörd, K. S., et al. (2024). Fracturing and tectonic stress drive ultrarapid magma flow into dikes. *Science*, *383*(6688), 1228–1235. https://doi.org/10.1126/science.adn2838

Sigmundsson, F., Vadon, H., & Massonnet, D. (1997). Readjustment of the Krafla spreading segment to crustal rifting measured by satellite radar interferometry. *Geophysical Research Letters*, *24*(15), 1843–1846. https://doi.org/10.1029/97GL01934

Smith, D., & Cann, J. (1993). Building the crust at the Mid-Atlantic Ridge. *Nature*, *365*(6448), 707–715. https://doi.org/10.1038/365707a0

Spaans, K., Hreinsdóttir, S., Hooper, A., Árnadóttir, T., & Pedersen, R. (2015). Crustal movements due to Iceland's shrinking ice caps mimic magma inflow signal at Katla volcano. *Scientific Reports*, *5*(1), 10285. https://doi.org/10.1038/srep10285

Sturkell, E., Sigmundsson, F., Geirsson, H., Ólafsson, H., & Theodórsson, T. (2008). Multiple volcano deformation sources in a post-rifting period: 1989–2005 behaviour of Krafla, Iceland constrained by levelling, tilt and GPS observations. *Journal of Volcanology and Geothermal Research*, *177*(2), 405–417. https://doi.org/10.1016/j.jvolgeores.2008.06.013

The GlaMBIE Team. (2025). Community estimate of global glacier mass changes from 2000 to 2023. *Nature*, *639*(3982), 382–388. https://doi.org/10.1038/s41586-024-08545-z

Toomey, D., Jousselin, D., Dunn, R., Williams, S. D. W., & Detrick, R. S. (2007). Skew of mantle upwelling beneath the East Pacific Rise governs segmentation. *Nature*, *446*(7134), 409–414. https://doi.org/10.1038/nature05679

Tryggvason, E. (1980). Subsidence events in the Krafla area, North Iceland, 1975–1979. *Journal of Geophysics*, *41*(1), 141–153. Retrieved from https://journal.geophysicsjournal.com/JofG/article/view/76

Tryggvason, E. (1984). Widening of the Krafla fissure swarm during the 1975–1981 volcano-tectonic episode. *Bulletin of Volcanology*, *47*(1), 47–69. https://doi.org/10.1007/BF01960540

Ulrych, T. J., Sacchi, M. D., & Woodbury, A. (2001). A Bayes tour of inversion: A tutorial. *Geophysics*, *66*(1), 55–69. https://doi.org/10.1190/1.1444923

Vaghri, A., & Hearn, E. H. (2012). Can lateral viscosity contrasts explain asymmetric interseismic deformation around strike-slip faults? *Bulletin of the Seismological Society of America*, *102*(2), 490–503. https://doi.org/10.1785/0120100347

Vardić, K., Clarke, P. J., & Whitehouse, P. L. (2022). A GNSS velocity field for crustal deformation studies: The influence of glacial isostatic adjustment on plate motion models. *Geophysical Journal International*, *231*(1), 426–458. https://doi.org/10.1093/gji/ggac047

Watson, A. R., Elliott, J. R., & Walters, R. J. (2022). Interseismic strain accumulation across the Main Recent Fault, SW Iran, from Sentinel-1 InSAR observations. *Journal of Geophysical Research: Solid Earth*, *127*(2), e2021JB022674. https://doi.org/10.1029/2021JB022674

Wessel, P., Luis, J. F., Uieda, L., Scharroo, R., Wobbe, F., Smith, W. H. F., & Tian, D. (2019). The Generic Mapping Tools version 6. *Geochemistry, Geophysics, Geosystems*, *20*(11), 5556–5564. https://doi.org/10.1029/2019GC008515

Wilcox, R. R. (2005). *Introduction to robust estimation and hypothesis testing* (2nd ed.). Elsevier Academic Press.

Williams, S. D. P. (2003). The effect of coloured noise on the uncertainties of rates estimated from geodetic time series. *Journal of Geodesy*, *76*(9–10), 483–494. https://doi.org/10.1007/s00190-002-0283-4

Wright, T. J., Parsons, B. E., & Lu, Z. (2004). Toward mapping surface deformation in three dimensions using InSAR. *Geophysical Research Letters*, *31*(1), L01607. https://doi.org/10.1029/2003GL018827

Wright, T. J., Sigmundsson, F., Pagli, C., Belachew, M., Hamling, I. J., Brandsdóttir, B., et al. (2012). Geophysical constraints on the dynamics of spreading centres from rifting episodes on land. *Nature Geoscience*, *5*(4), 242–250. https://doi.org/10.1038/ngeo1428

Yang, Y., Sigmundsson, F., & Geirsson, H. (2023). Joint Bayesian modeling of velocity break points, noise characteristics, and their uncertainties in GNSS time series: Far-field velocity anomalies concurrent with magmatic activity in Iceland. *Geophysical Research Letters*, *50*(14), e2023GL103432. https://doi.org/10.1029/2023GL103432

Yang, Y., Sigmundsson, F., Geirsson, H., Biggs, J., Drouin, V., Sepúlveda Araya, J., et al. (2026). Long-term ground deformation velocity fields from GNSS (2002–2024) and Sentinel-1 InSAR (2015–2023) at the Krafla volcanic system, Iceland [Dataset]. *Zenodo*. https://doi.org/10.5281/zenodo.18528356

Yang, Y., Sigmundsson, F., Geirsson, H., & Gottsmann, J. (2025). Role of tectonic stress and topography on repeated lateral dikes: Application to the 1975–1984 Krafla and 2023–2025 Svartsengi rifting episodes in Iceland. *Bulletin of Volcanology*, *87*(12), 105. https://doi.org/10.1007/s00445-025-01897-y

Yu, C., Li, Z., Penna, N. T., & Crippa, P. (2018). Generic atmospheric correction model for interferometric synthetic aperture radar observations. *Journal of Geophysical Research: Solid Earth*, *123*(10), 9202–9222. https://doi.org/10.1029/2017JB015305

Yuan, T., & Zhong, S. (2025). Effects of glacial forcing on lithospheric motion and ridge spreading. *Nature*, *641*(122), 122–128. https://doi.org/10.1038/s41586-025-08846-x

21699356, 2026, 8, Downloaded from https://agupubs.onlinelibrary.wiley.com/doi/10.1029/2026JB034040 by Technical University Delft, Wiley Online Library on [02/09/2026]. See the Terms and Conditions (https://onlinelibrary.wiley.com/terms-and-conditions) on Wiley Online Library for rules of use; OA articles are governed by the applicable Creative Commons License